Characterization of dynamic hardening behavior at intermediate strain rates using the Virtual Fields Method

Jin-Seong Park[a,b], Ji-Min Kim[a], Frédéric Barlat[a], Ji-Ho Lim[c], Fabrice Pierron[d], Jin-Hwan Kim[a,*]

[a] GIFT, Pohang University of Science and Technology, 77 Cheongam-ro, Nam-gu, Pohang, Gyeongbuk 37673, Republic of Korea

[b] LG Chem, 188 Munji-ro, Yuseong-gu, Daejeon 34122, Republic of Korea

[c] Steel Solution Research Laboratory, POSCO, 100 Songdo Gwahak-ro, Yeonsu-gu, Incheon 21985, Republic of Korea

[d] Faculty of Engineering and Physical Sciences, University of Southampton, University Road, Southampton SO17 1BJ, United Kingdom

*Corresponding author: Jin-Hwan Kim
Phone: +82 54 279 9058
E-mail: jinkim@postech.ac.kr
Full postal address:
GIFT, Pohang University of Science and Technology,
77 Cheongam-Ro, Nam-Gu, Pohang, Gyeongbuk, 37673, Republic of Korea

ABSTRACT

Crash analysis simulation is now very important in automotive industry to assess automotive crashworthiness and safety. In order to acquire reliable crash simulation results, precise material behaviors at intermediate strain rates should be used as input data. To derive the stress-strain curves at various strain rates, a large number of experiments are needed, which is costly and time consuming. The present study aims at determining the stress-strain curves of sheet metals at various strain rates from a single dynamic experiment. A new type of high-speed tensile tester for sheet metal specimens was built and high-speed tensile tests were carried out. Full-field heterogeneous strain fields were measured by a digital image correlation technique using a high-speed camera. The load data was acquired from strain gauges attached to the elastic deformation region on the specimen. Then, an inverse identification scheme with a rate dependent hardening law was applied to retrieve dynamic parameters. The stress-strain curves of three advanced high strength steels at intermediate strain rates (100 s^{-1} – 300 s^{-1}) were successfully obtained from a single experiment.

Keywords: Dynamic hardening behavior; Sheet metal; Intermediate strain rates; The virtual fields method (VFM); Digital image correlation (DIC)

1. Introduction

Safety and environmental issues are major concerns for automobile companies at present, and the regulations surrounding these issues are being strengthened in many countries around the world. To meet regulations, automobile companies are striving to utilize lightweight and strong materials to optimize the design of vehicle structures. As a solution, advanced high strength steel (AHSS) is widely used for car body structures because AHSS has higher strength than conventional steel. The usage of AHSS not only enhances safety, but also makes it possible to optimize car body design, which can greatly reduce its weight.

Before bringing new cars to market, vehicle safety tests such as crash tests, should be performed by an authorized inspection agency. However, because it is expensive to perform multiple actual crash tests during the design process, automotive companies generally perform virtual tests using finite element analysis (FEA). FEA is very cost-effective and time-efficient when applied to the analysis of structures. In order to acquire trustworthy automobile crash simulation results, precise material behaviors at intermediate strain rates should be fed as input. The true stress-strain curves at various intermediate strain rates are the fundamental information for the input data.

Many experimental systems have been devised for the identification of dynamic properties at high rates of deformation (Field et al., 2004), and among them, servo-hydraulic high-speed tensile machines have been usually used for acquiring the stress-strain curve data at intermediate strain rates (Borsutzki et al., 2005).

Commonly, the mechanical properties of the material change depending on the strain rate and for automotive AHSS, as the strain rate increases, the flow stress tends to increase (POSCO, 2014). Therefore, in order to determine the stress-strain curves at various strain rates, the number of required experiments increases significantly. In addition, it is desirable to characterize dynamic behavior at specific strain rates used for the FE simulation. However, experiments involving high deformation rates are strongly influenced by inertia effects (Pierron et al., 2011). In an Instron servo-hydraulic high-speed tensile tester, the average strain rate along the gauge length of a specimen fluctuates during dynamic deformation as shown in Fig. 1.

The target strain rate is 200 s^{-1} and variance of the strain rate is around 100 s^{-1} in this case. Average strain rate can be used by smoothing the fluctuating strain rate, but there is no guarantee that the obtained engineering stress-strain curve describes the hardening behavior at a specific strain rate correctly. Furthermore, several studies reported the temporal and spatial variations of strain rate in dynamic testing (Avril et al., 2008b; Pierron et al., 2011; Koohbor et al., 2016; Fletcher et al., 2021). Thus, it is a very challenging task to determine initial yield stress and flow stress at a given strain rate.

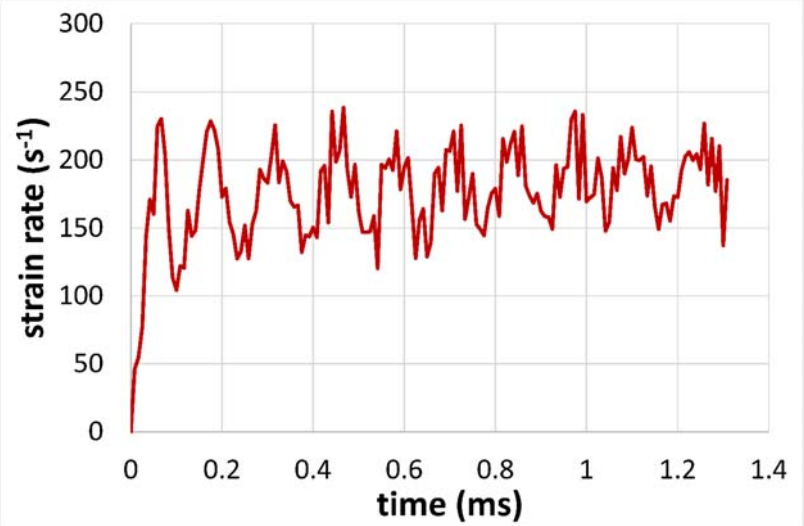

Fig. 1. Evolution of average strain rate during the dynamic deformation (target strain rate: 200 s^{-1}).

In order to solve the varying strain rate problem, some researchers developed a new technique in which the relationship between stress and strain rate is calculated as a function of plastic strain from numerous experimental data (Bae, 2013; Huh et al., 2014). Then, the strain rate sensitivity is retrieved using a rate dependent hardening model by fitting the stress with respect to increasing strain rate for a designated plastic strain. Finally, the stress-strain curve at a specific strain rate can be drawn by recombining this information. Koohbor et al. (2016) used a similar approach to acquire the stress-strain curves of polymeric foam specimens at various strain rates. This method can provide more reasonable data, however, the data-processing involved with this method is quite complicated, and the procedure requires significant amount of time-consuming experimentation.

The present study aims at proposing a new method to overcome the problems mentioned above efficiently. The idea is to determine the strain rate dependence by taking advantage of heterogeneity of

strain rate measured from full-field deformation measurements.

The idea is based on the study of Avril et al. (2008b) in which the elasto-visco-plastic behavior was characterized from a single test by exploiting the heterogeneous strain rate information. A tensile load was applied on a notched mild steel specimen and the parameters of modified Perzyna's model were retrieved at strain rates ranging from 0.1 to 10 s^{-1}. Based on this pioneer works, several researches have been carried out to identify the rate dependent constitutive response of various materials from a single experiment using the heterogeneous strain rate information. Stress-strain responses of cylindrical polymeric foam specimens were acquired over strain rates from 1000 to 5000 s^{-1} by applying impact loading (Koohbor et al., 2016) and Johnson-Cook model parameter was identified from an impacted copper specimen using dynamic three point bending tests (Koohbor et al., 2017). Seghir et al. (2017) identified Young's modulus variation of a polymer specimen (PMMA) at strain rates of 10 to 200 s^{-1} by using ultrasonic tests. Recently, several attempts were made to identify the parameter of rate dependent hardening laws using image-based inertial impact (IBII) tests (Pierron et al., 2014). The IBII test can generate the tensile stress by impacting one edge of a rectangular specimen. A computational approach was used to optimize the IBII tests for the characterization of the dynamic behavior of metals at high strain rate by increasing the strain rate heterogeneity (Bouda et al. 2019) and Fourest et al. (2020) determined the Johnson-Cook model parameter of titanium alloy. The parameters of the hardening laws (linear and Voce) for stainless steel at different strain rates were determined using the heterogeneous strain rate information (Fletcher et al. 2021).

The purpose of this study is to determine the stress-strain curves of AHSS at intermediate strain rates (100 s^{-1} – 300 s^{-1}) from a single dynamic experiment using a new type of high-speed tensile tester. The main idea of identifying the stress-strain curves at various strain rates from a single experiment is based on the observation that the strain rate distribution is heterogeneous over the area of interest of the specimen. This means that rich strain rate information can be used for the identification of strain rate dependence. In this study, dynamic hardening properties of thin steel sheet specimens at intermediate strain rates are identified by using the virtual fields method (VFM) (Pierron and Grédiac, 2012) with a rate dependent hardening law. The VFM is an inverse analytical tool for deriving the mechanical

properties of materials based on the principle of virtual work.

Several applications of the VFM to elasto-plastic problems have been carried out successfully for quasi-static deformation (Avril et al., 2008a; Pierron et al., 2010; Rossi and Pierron, 2012; Kim et al., 2013; Kim et al., 2014; Fu et al., 2017). For dynamic deformation in elasto-plasticity, the VFM was applied to identify the constitutive parameters of rate dependent models at low deformation rate (Avril et al., 2008b; Notta-Cuvier et al., 2013) and Notta-Cuvier et al. (2013) showed the possibility of the VFM to determine the viscoplastic parameters of Johnson-Cook model. For high rate deformation in elasto-plasticity, the main focus has been on retrieving dynamic properties without measuring load by using the acceleration field as load information through the equilibrium equation (Pierron et al., 2014; Le Louëdec et al., 2015; Grama et al., 2015; Koohbor et al., 2017; Bouda et al., 2019; Fourest et al., 2020).

In this study, the VFM is adopted to determine the true stress-strain curves at intermediate strain rates, which are very important for car crash simulation in practice. A new type of high-speed tensile tester for sheet metal specimens was built and high-speed tensile tests were performed. Digital image correlation using a high-speed camera was utilized to measure strain fields so that the identification is carried out from the measured quantities. An advanced rate dependent hardening law was chosen to derive the stress-strain curves at various intermediate strain rates. First, the proposed methodology is introduced and the VFM-based identification procedure with a rate dependent model is validated using FE simulation. After the validation, the preparatory work and data processing methods to be applied to the actual experiment are explained. Finally, experimental results are shown and some aspects of the results are analyzed.

2. Methodology

2.1 Impact frame high-speed (IFHS) tensile tester

For the experiments, a novel high-speed tensile tester for sheet metal materials based on Tran and Kim (2012) has been developed, and the experimental set-up is shown in Fig. 2. A schematic illustrating the principle of the tester is presented in Fig. 3. In the high-speed tensile tester, two metallic frame bars

are connected to a hydraulic pump through a coupler, which is designed to fail when the load exceeds its capacity. When the pump starts to impose tensile load on the coupler as in Fig. 3(a), the coupler endures the load until it reaches to critical load value and elastic strain energy is accumulated in the frame bars at the same time. If the load is increased to break the coupler as in Fig. 3(b), the energy within the frame bars is released so that the specimen connected to a frame module is pulled in tension at high deformation rate as in Fig. 3(c). The tester has several advantages, including relatively low cost compared with other types of dynamic tensile testers and the possibility to generate intermediate strain rates up to 300 s^{-1} for advanced high strength steel specimens. The strain rate during the test can be controlled by changing the design of the coupler and frame bars.

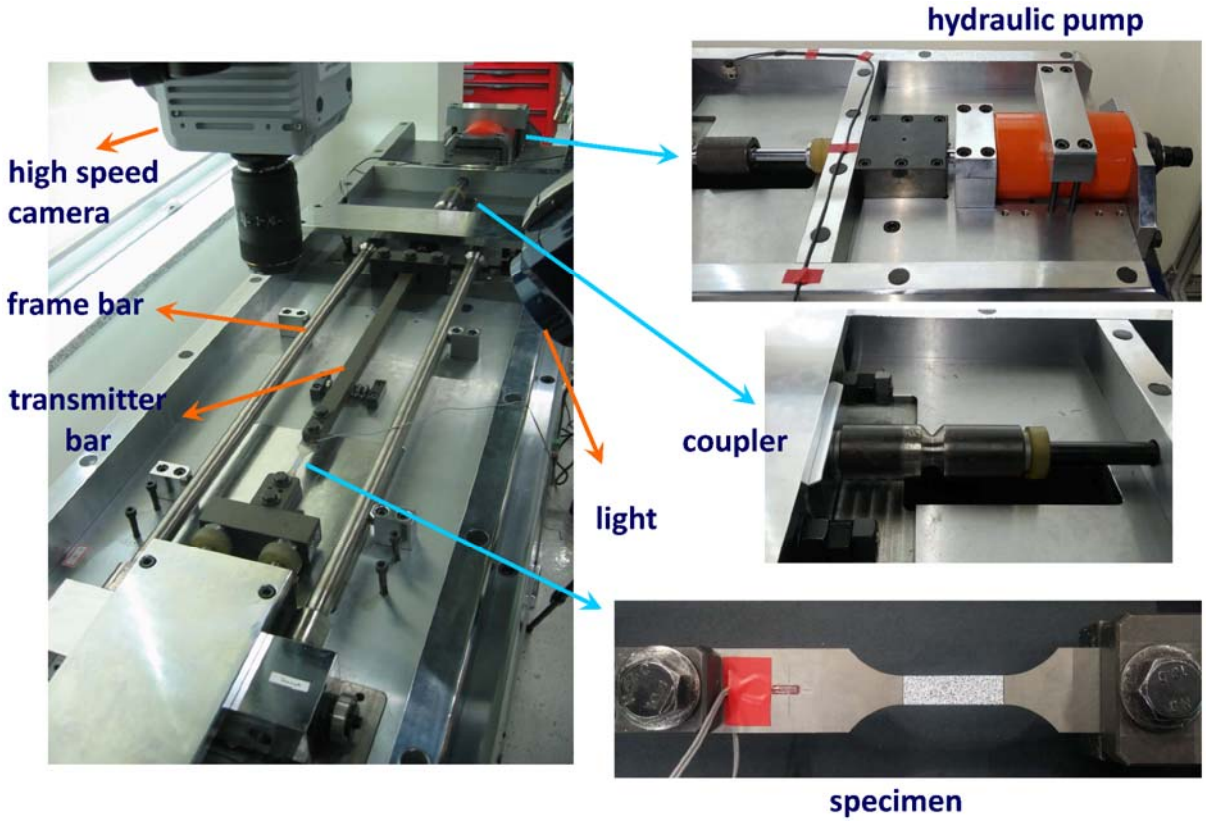

Fig. 2. The experimental set-up for sheet metal IFHS tests.

A special “dog-bone” type specimen was used for the IFHS tester, as illustrated in Fig. 4. The holes on one grip side are round, and the holes on the other side are rounded rectangular. The grip side with the circular holes is fixed to the transmitter bar. The other end is connected to the frame bar module so that the specimen is pulled when the frame bar moves.

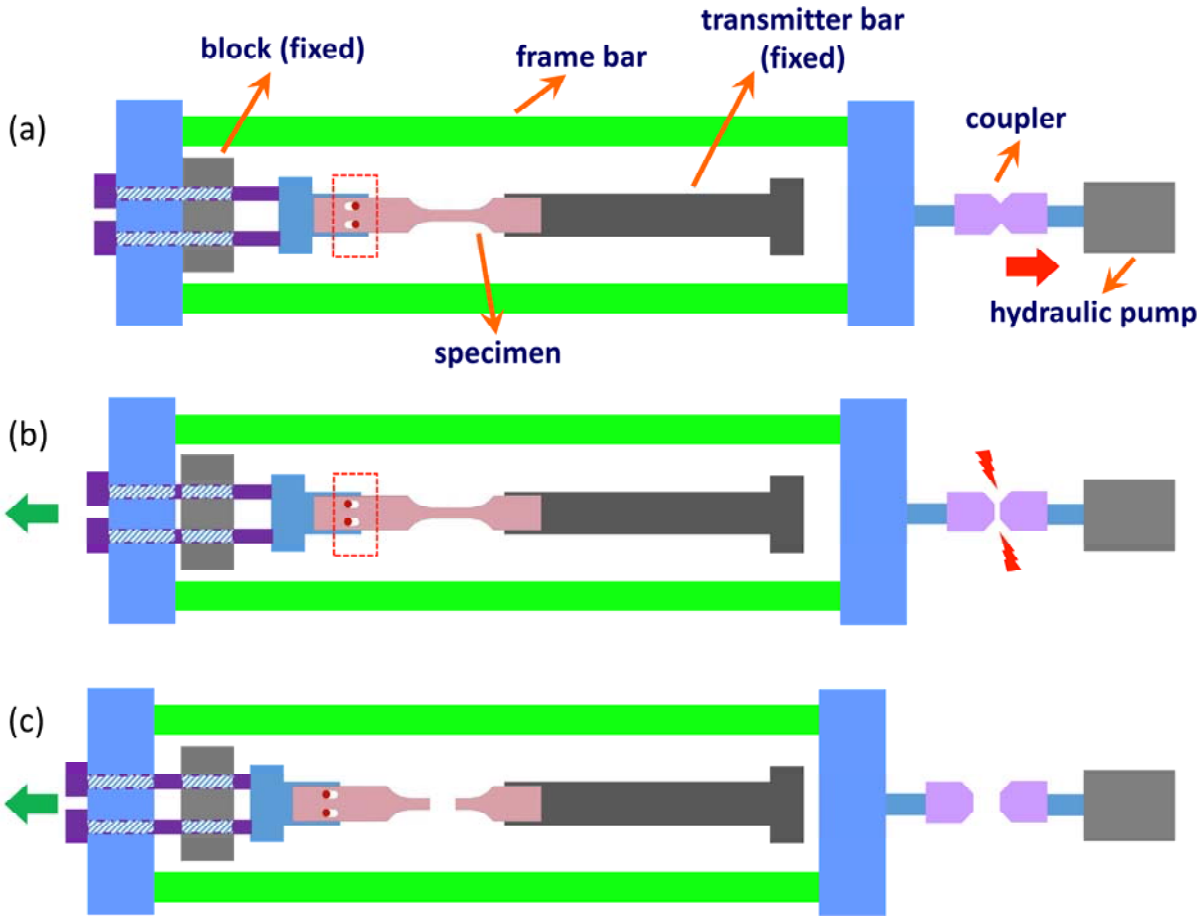

Fig. 3. A schematic illustrating the principle of the tester.

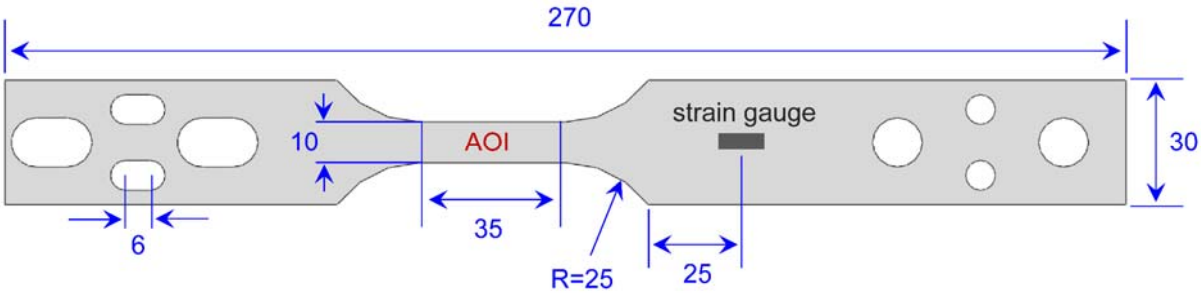

Fig. 4. Specimen geometry for the IFHS tests (unit: mm).

It is worth noting here that in the current test set-up, specimen gripping was modified as shown in Fig. 5. In the case of the original circular holes, the specimen is pulled from the very beginning of the cross-head movement and this mitigates the initial acceleration, leading to low strain rate ramp. By changing the circular holes to rounded rectangles, the specimen is pulled after certain speed is reached

as described in Fig. 3(a) and Fig. 3(b) (red-dotted rectangle) and Fig. 5. This is a similar design of the slack adaptor used on Instron VHS machines, for instance Longana et al. (2009).

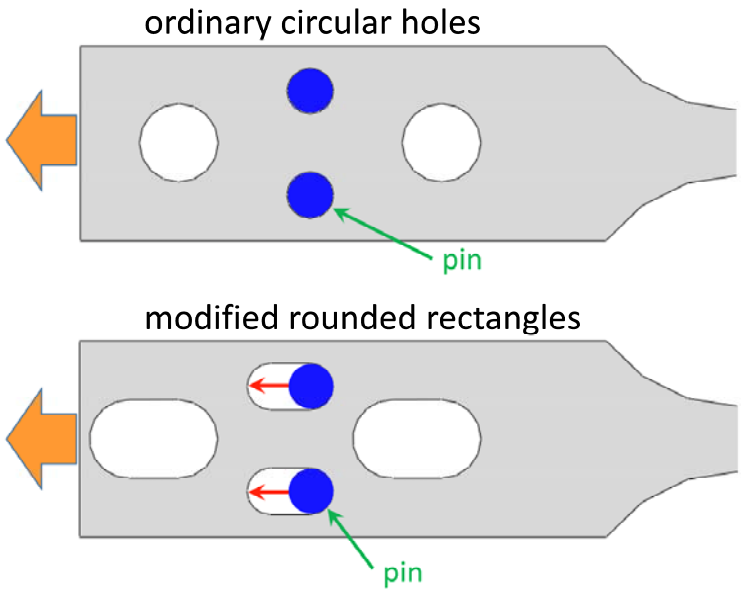

Fig. 5. Modification of grip condition.

For the experimental application, three advanced high strength steel (AHSS) grades with different strain hardening behaviors were chosen in this study, namely, dual-phase DP590, DP780 and DP980 with the thickness of 1.4, 1.4 and 1.2 mm, respectively. All the specimens were cut in the rolling direction.

2.2 Digital image correlation (DIC) with a high-speed camera

In the experiments, high-speed tensile tests on sheet metal specimens were conducted and full-field in-plane displacement fields were measured by a digital image correlation (DIC) technique (Sutton et al., 2009) using a high-speed camera (Photron FASTCAM SA-X2). The high-speed camera took images of the speckle patterns at 120,000 frame per second (fps) with the pixel size of 640 × 128.

The parallel gauge section was selected as the area of interest (AOI) and random speckle patterns were drawn for DIC analysis by applying black dots on matt white paint as a base. The initial size of the AOI was 10 mm (width) × 35 mm (initial gauge length). Measurement points (blue point) from the

DIC measurement are shown in Fig. 6. The Vic-2D software (www.correlatedsolutions.com) was used for DIC analysis. A subset size of 21 pixels and a step size of 5 pixels were used and the physical image pixel size was 0.089 mm. The information on DIC parameters is presented in Table 1.

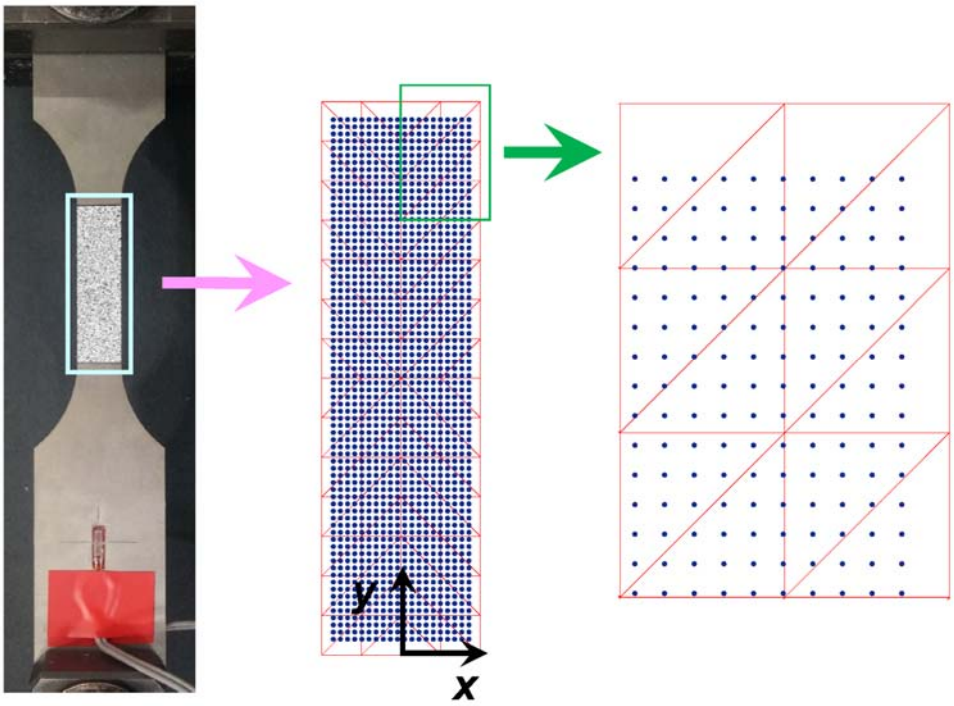

Fig. 6. Speckle patterns on AOI and measurement points from DIC Analysis.

In order to calculate the logarithmic strain fields to be used for large deformation analysis, the exact AOI dimension was obtained from a FE software and the whole AOI was meshed using triangular elements as shown in Fig. 6. The undeformed coordinates of nodal points in each triangle element were known and the deformed coordinates of nodal points at each loading stage were calculated from the undeformed and deformed coordinates of DIC measurement points using the analytical approach adopted in Kim et al. (2013). This procedure is carried out by least squares regression (Kim et al., 2014). Then, the deformation gradient F for each triangle was retrieved using the theory of finite deformation (Dunne and Petrinic, 2005). A plane stress state and incompressibility $(\det(F) = 1)$ in plasticity were assumed. Then the logarithmic strain tensor ε_{ln} was obtained from the deformation gradient F through the right stretch tensor U $(U^2 = F^T F)$ as in Eq. (1).

$$\varepsilon_{ln} = \sum_{i=1}^{3} \ln(\lambda_i) r_i \otimes r_i \tag{1}$$

where λ_i and r_i are the eigenvalues and eigenvectors of the right stretch tensor U respectively.

The strain resolution was obtained by calculating the standard deviation of the logarithmic strains from 21 successive undeformed images. The measured strain resolution were 6.44 $\times$ 10^{-5} (ε_{xx}), 3.63 $\times$ 10^{-5} (ε_{yy}) and 3.91 $\times$ 10^{-5} (ε_{xy}) for in-plane strains.

From the calculated strain components in each triangle element, the strain rate $\dot{\varepsilon}$ in each element can be obtained at each time step.

$$\dot{\varepsilon}_i \left(t + \frac{\Delta t}{2} \right) = \frac{\varepsilon_i(t + \Delta t) - \varepsilon_i(t)}{\Delta t} \tag{2}$$

where i is x, y or xy and t is time.

The velocity v in each triangle element can be calculated from the measured displacement u using simple finite difference.

$$v_j \left(t + \frac{\Delta t}{2} \right) = \frac{u_j(t + \Delta t) - u_j(t)}{\Delta t} \tag{3}$$

where j can be either x or y.

The acceleration a in each triangle element can be computed from the displacement u by second order finite differences as in Eq. (4). Due to the nature of the dynamic quantities, the velocity is calculated at time $t + \frac{\Delta t}{2}$ and the acceleration at time t.

$$a_j(t) = \frac{u_j(t + \Delta t) + u_j(t - \Delta t) - 2u_j(t)}{\Delta t^2} \tag{4}$$

At this stage, an important idea adopted in this study to identify the stress-strain curves at various strain rates from a single dynamic experiment will be introduced. As can be seen in Fig. 7(a), though the average strain rate from the whole AOI is quite constant at around 200 s^{-1}, the strain rate distribution is non-uniform over the AOI. The strain rate distribution from each triangle element varies from around 100 s^{-1} to 300 s^{-1} as shown in Fig. 7(b). This means that this rich strain rate information can be fed into the VFM to identify strain rate dependence with an appropriate rate dependent model.

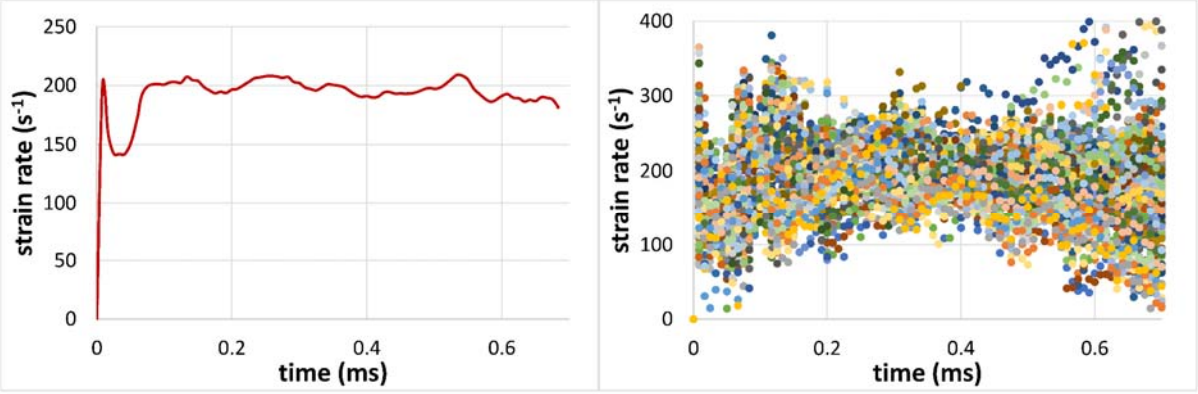

Fig. 7. Evolution of (a) AOI-averaged strain rate and (b) strain rates at all triangular elements (strain rate distribution) in the AOI obtained from the IFHS tester.

Table 1

Imaging and measurement performance information (DP590).

Technique used	Digital Image Correlation
Camera	Photron FASTCAM SA-X2
Sensor and digitization	1024 × 1024 pixels, 12-bit
Lens, imaging distance	Sigma 105mm Macro Lens, 390 mm
Total number of images (elapsed time)	180 (1.5 ms)
Frame per second (fps)	120,000
Pixel size	640 × 128
Pixel to mm conversion	1 pixel = 0.089 mm
Subset (SS), step (ST)	21, 5
Interpolation, shape functions, correlation criterion	Cubic spline, affine, Normalized squared differences
Strain	
Smoothing technique	Local polynomial
Strain window (SW)	20 data points
Resolution	6.44×10^{-5} (ε_{xx}), 3.63×10^{-5} (ε_{yy}) and 3.91×10^{-5} (ε_{xy})

2.3 Constitutive model

Choosing a constitutive model which can describe the dynamic strain hardening behavior properly is

important. In this study, von Mises yield criterion under plane stress and Lim-Huh model (Huh et al., 2014) for an advanced rate dependent hardening law were chosen to retrieve the relationship between stress and strain. The associated flow rule was assumed.

The yield condition can be written as:

$$f(\sigma, \varepsilon_p) = \sigma_{eq}(\sigma) - \sigma_s(\varepsilon_p) = 0 \tag{5}$$

where σ_{eq} is the von Mises equivalent stress, σ_s current yield stress and ε_p is the equivalent plastic strain.

The Lim-Huh model is composed of quasi-static and dynamic terms and can be written as follows:

$$\sigma_s(\varepsilon_p) = \sigma_r \frac{1 + q(\varepsilon_p)\dot{\varepsilon}_{p,d}^m}{1 + q(\varepsilon_p)\dot{\varepsilon}_{p,r}^m} \quad \text{where} \quad q(\varepsilon_p) = q_1(\varepsilon_p + q_2)^{-q_3} \tag{6}$$

where σ_r and $\dot{\varepsilon}_{p,r}$ are the flow stress and the equivalent plastic strain rate at quasi-static state and $\dot{\varepsilon}_{p,d}$ is the dynamic equivalent plastic strain rate. Any hardening equation can be used for σ_r.

The advantage of Lim-Huh model is that it consists of two strain rate sensitivities of q and m, and q varies depending on evolution of strain. In contrast, the strain rate sensitivity parameter C in Johnson-Cook model in Eq. (7) is a constant.

$$\sigma_s = \sigma_r \left(1 + C \ln\left(\frac{\dot{\varepsilon}_{p,d}}{\dot{\varepsilon}_{p,r}}\right)\right) \tag{7}$$

Consequently, it is considered that Lim-Huh model has more flexibility to describe suitably the complex dynamic hardening behavior. In this study, the strategy to identify the material parameters of the Lim-Huh model is that the hardening parameters of σ_r are determined from standard uniaxial tensile tests at quasi-static and the four dynamic parameters (q_1, q_2, q_3 and m) are identified by the VFM using dynamic experimental measurements to reduce the number of parameters to be identified with the VFM.

In the von Mises yield criterion under plane stress, the relationship between the stress increment and the total strain (ε_t) increment can be derived from the plasticity theory using the associated flow rule, the consistency condition, and elastic-plastic strain decomposition (Chen, 1994; Dunne and Petrinic,

2005; Kim et al., 2013). The relationship is expressed in the incremental form because stress is history dependent in plasticity.

$$\{d\sigma\} = \left([C] - \frac{[C]\left\{\frac{\partial f}{\partial \sigma}\right\}^T \left\{\frac{\partial f}{\partial \sigma}\right\}[C]}{\left\{\frac{\partial f}{\partial \sigma}\right\}^T [C]\left\{\frac{\partial f}{\partial \sigma}\right\} - \left\{\frac{\partial f}{\partial \varepsilon_p}\right\}\sqrt{\frac{2}{3}\left\{\frac{\partial f}{\partial \sigma}\right\}^T \left\{\frac{\partial f}{\partial \sigma}\right\}}} \right) \{d\varepsilon_t\} \quad (8)$$

where $[C]$ corresponds to the elastic stiffness matrix, and the terms in $\{\ \}$ are vector quantities with three in-plane components (plane stress assumption).

The calculation of the stress increment requires the derivation of the current yield stress σ_s with respect to the equivalent plastic strain ε_p as shown by Eqs. (5) and (8). Since the rate dependent hardening law includes the equivalent plastic strain rate term ($\dot{\varepsilon}_p = d\varepsilon_p/dt$), the derivation is not straightforward. The calculation of the derivation of $d\sigma_s/d\varepsilon_p$ is shown in Appendix A.

2.4 The virtual fields method

In this study, the virtual fields method (VFM) was employed as an inverse method to retrieve the constitutive parameters from the measured full-field deformation fields. The VFM makes use of the principle of virtual work which describes the condition of global equilibrium. The equilibrium equation in the case of elasto-plasticity for dynamic loading, and in absence of body forces, can be written as follows:

$$-\int_V \left[\int_0^t \frac{d\sigma_{ij}}{dt} dt\right] \varepsilon_{ij}^* dV + \int_{S_f} T_i u_i^* dS = \int_V \rho a_i u_i^* dV \quad (9)$$

where $d\sigma/dt$ is the stress rate tensor which is a function of $\dot{\varepsilon}$, σ and unknown constitutive parameters, V the measurement volume, T the distribution of applied forces acting on the boundary of the specimen S_f, ε^* the virtual strain field derived from u^* (the virtual displacement field, which has to be continuous and piecewise differentiable), ρ the density and a the acceleration. The summation convention applies on repeated indices.

The equilibrium equation indicates that the external virtual work (EVW) including external surface

traction T equals the sum of the internal virtual work (IVW) with the stress information $d\sigma/dt$ and the acceleration virtual work (AVW) with the acceleration information a. The AVW can be neglected in the case of quasi-static state because acceleration is close to zero, however at high strain rates, the AVW should be considered for the VFM analysis because the acceleration effect is not negligible.

For an elasto-plasticity problem, it is necessary to take the entire loading history into account for the identification which has to be carried out using an iterative procedure (Grédiac and Pierron, 2006) to minimize the quadratic gap between the IVW and (the EVW $-$ the AVW) at each loading stage. Since the constitutive parameters are unknown, initial guesses are required to initiate the iterative process. Then, the stress increments are recalculated at each stage (time step) using the radial return algorithm proposed by Sutton et al. (1996) until the equilibrium equation is satisfied. Non-linear least squares algorithm (lsqnonlin) in Matlab was used for the minimization.

Appropriate virtual fields should be chosen to identify the dynamic parameters. Virtual displacement fields should be continuous and piecewise differentiable over the AOI. In this study, simple virtual fields were applied to find the material parameters as in Eq. (10).

$$u_{\mathrm{x}}^{*} = 0,\ u_{\mathrm{y}}^{*} = y \quad \text{thus} \quad \varepsilon_{\mathrm{xx}}^{*} = 0,\ \varepsilon_{\mathrm{yy}}^{*} = 1,\ \varepsilon_{\mathrm{xy}}^{*} = 0 \tag{10}$$

where x and y are the horizontal and vertical coordinates as in Fig. 6.

3. Simulation

The main purpose of the simulation was to check that the chosen rate dependent model was implemented in the VFM identification routines correctly and to validate the feasibility of the VFM for the identification of dynamic parameters of the Lim-Huh model. Virtual measurements were acquired from the FE software Abaqus/Explicit. The identification was performed using the same procedure adopted for the experiments.

3.1 Finite element (FE) model

The FE model with the geometry corresponding to the actual specimen was constructed as shown in Fig. 8. In order to mimic the scattered measurement points from DIC, 4-node shell elements with

reduced integration (S4R) with fine mesh size of 0.3 mm were used. The area of interest (AOI) was chosen identical to that of the experiments, as the central region with 35 mm gauge length. The deformed nodal coordinates of each element were saved at evenly spaced time intervals (100 loading steps). The AOI was meshed using triangular elements as shown in section 2.2 and the logarithmic strain and acceleration fields were derived from the triangular elements at each measurement step. The load data was calculated from the reaction force on the lower edge in Fig. 8. The thickness of the specimen was 1.0 mm.

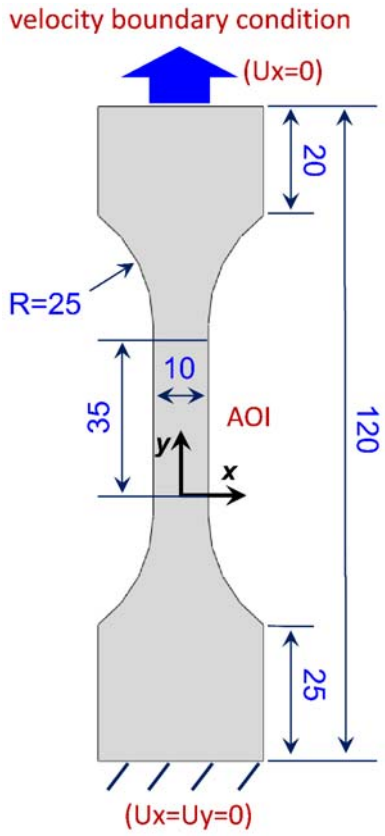

Fig. 8. The FE model for the IFHS test simulations (unit: mm).

In order to simulate the actual experimental loading condition, the pulling velocity at one edge of the specimen in the impact frame high-speed (IFHS) tensile test was measured. Speckle patterns were made on the pulling side of the specimen, as depicted in Fig. 9(a) and the specimen was pulled dynamically using the IFHS tester. Fig. 9(a) shows the area (red rectangle) where the velocity information was extracted and the measured velocity in Fig. 9(b) was fed into the FE simulations as the velocity

boundary condition.

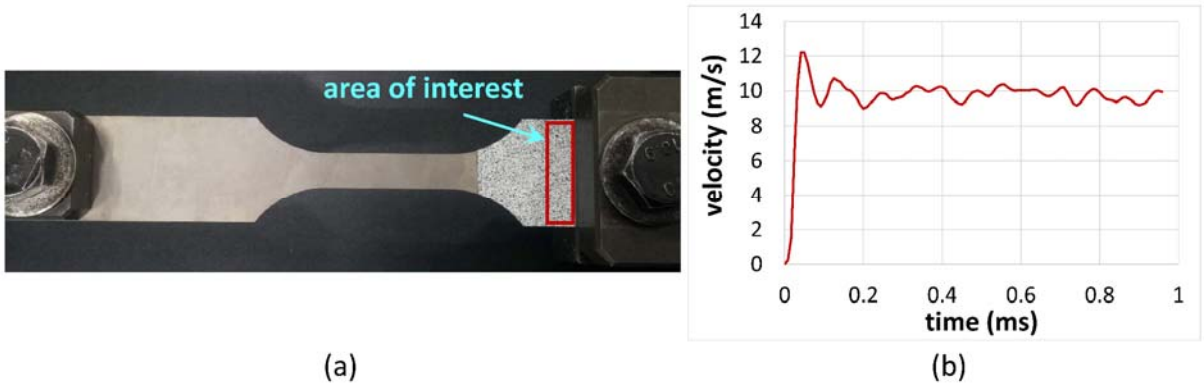

Fig. 9. Measurement of velocity for FE boundary condition (a) speckle patterns on the pulling side (b) evolution of velocity at the pulling part of the specimen.

3.2 Validation of the VFM with Johnson-Cook model

First, Johnson-Cook model in Eq. (7) was adopted since Johnson-Cook model is implemented in Abaqus. The specific chosen input parameters in the FE simulations are presented in Table 2. The parameters of the quasi-static hardening term σ_r in Eq. (7), here Swift model in Eq. (11), were given as known values because these parameters can be easily derived from a quasi-static experiment. Only the dynamic parameter C was identified through the application of the VFM.

$$\sigma_r = X_1\left(X_2 + \varepsilon_p\right)^{X_3} \tag{11}$$

Simulations were conducted for a material with density of 7,800 kg/m^3, elastic modulus of 200 GPa, and Poisson's ratio of 0.3, and assumed to follow the isotropic von-Mises yield criterion.

Table 2

Input parameters in the FE simulations for the Johnson-Cook model.

X_1 (MPa)	X_2	X_3	C	$\dot{\varepsilon}_{p,r}$ (s^{-1})
1430	0.0021	0.157	0.03	0.001

The AOI-averaged strain rate, velocity, acceleration and the load data (reaction force from the lower edge in Fig. 8) as a function of time are shown in Fig. 10. Acceleration occurs because the deformation

velocity changes rapidly at the initial time steps, however, the acceleration is nearly zero in the hardening region because the deformation velocity is nearly constant. It should be noted once again that, in Fig. 10(b), the dots with different colors along the vertical axis indicate the strain rate distribution from each triangle element in Fig. 6 at each time step.

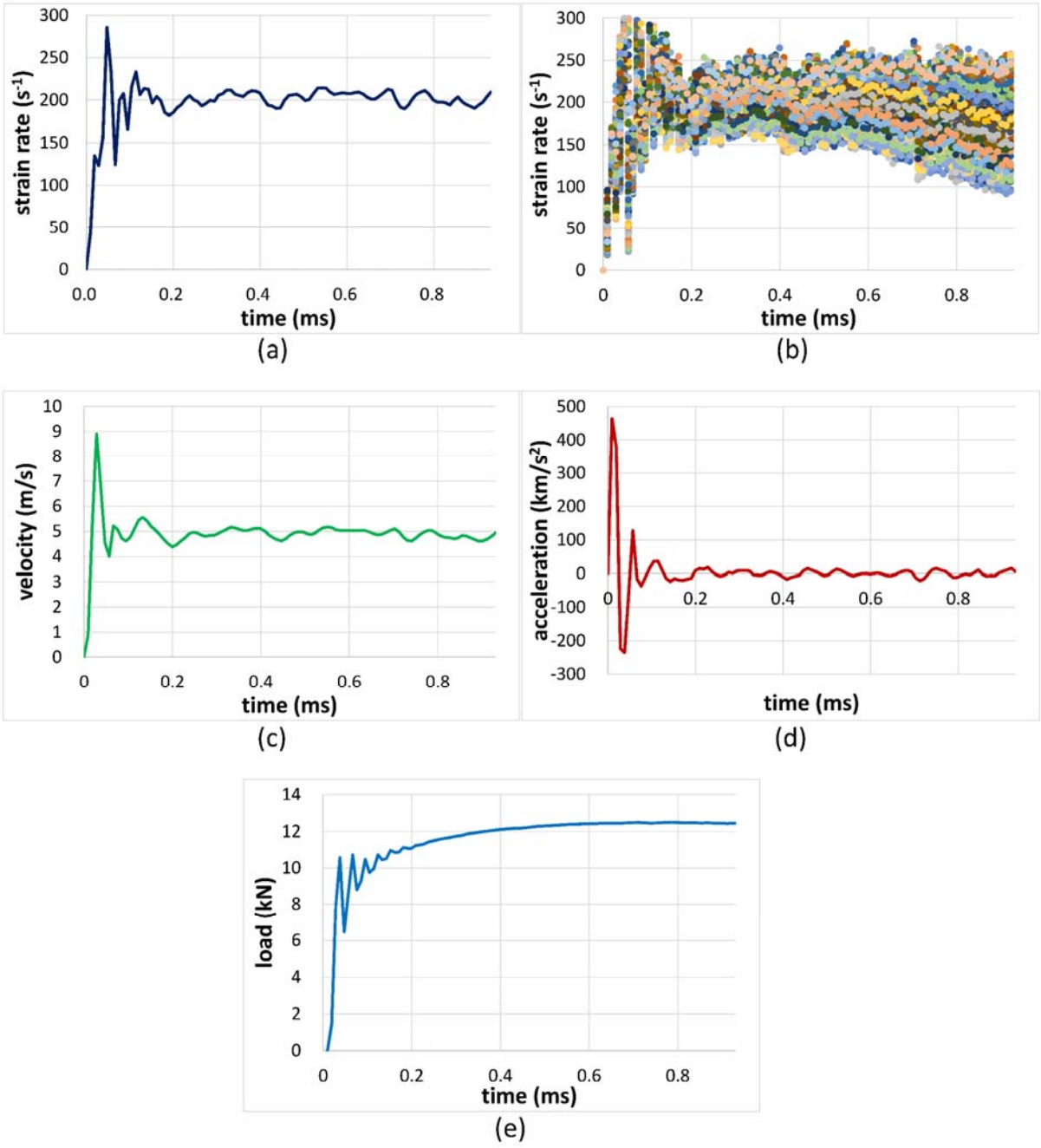

Fig. 10. Evolution of (a) AOI-averaged strain rate (b) strain rate distribution (c) AOI-averaged velocity (d) AOI-averaged acceleration (e) load in the loading direction (FE simulation).

The strain, strain rate, and acceleration information were input into the VFM and the dynamic parameter C was identified as shown in Table 3. Though the relative error of the identified Johnson-Cook parameter is 2.87 %, the relative errors between the calculated flow stresses from the identified parameter and the reference stresses are less than 1% at the strain rates of 100 s^{-1}, 200 s^{-1} and 300 s^{-1}.

Table 3

Identified Johnson-Cook model parameter value (FE simulation, R.E: relative error).

Johnson-Cook model parameter	C
input	0.03
identified	0.03086
R.E.	-2.87 %

The balancing result of three virtual works after convergence is shown in Fig. 11. It can be seen that the EVW is dominant at intermediate strain rates. Though the effect of the AVW is not significant for the identification, the AVW was also taken into account for the identification in this study.

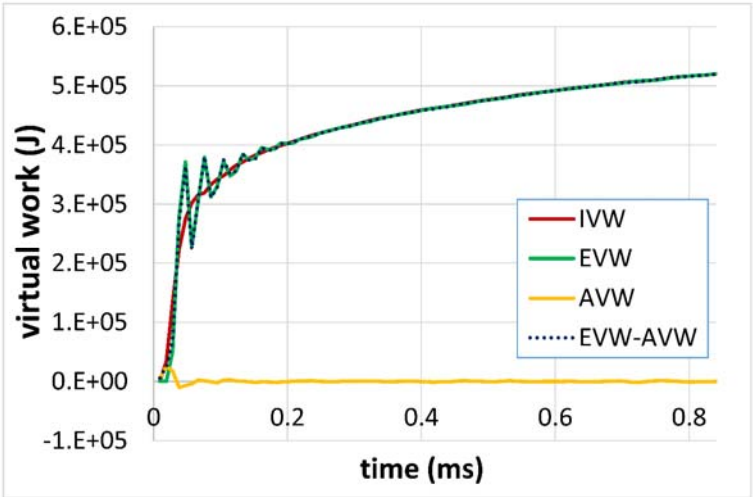

Fig. 11. The virtual work balancing result after convergence (FE simulation).

3.3 Validation of the VFM with Lim-Huh model

The next step was to identify Lim-Huh model parameters using the VFM. Because the Lim-Huh model is not implemented in Abaqus, the Johnson-Cook model was used for the FE analysis and the

material parameters were derived from the VFM with Lim-Huh model.

The Lim-Huh model parameters identified by the VFM are listed in Table 4. Three different initial estimates were used to check the existence of a unique solution for the Lim-Huh model. It was found that there exist many local optima depending on the initial estimates as can be seen in Table 4 whereas the Johnson-Cook model provides a global optimum regardless of the initial estimates. However, the calculated flow stresses from the determined parameters are very close to each other and also match well with the reference stress at the strain rate of 200 s^{-1} as shown in Fig. 12. Appropriate upper bounds and lower bounds were chosen based on the study of Lim (2005) to expedite the iteration procedure for the identification and those are listed in Table 5. The selected bounds will also be used for the identification with the experimental data. The concern of FE simulation was to verify the identification procedure using the VFM and the dynamic parameters of rate dependent models were successfully identified.

Table 4

Identified Lim-Huh model parameters from the VFM (FE simulation).

Lim-Huh model parameter	q_1	q_2	q_3	m
initial estimate 1	0.1	0.1	0.1	0.1
identified 1	1.066	0.1797	0.05439	0.05019
initial estimate 2	1	0.01	0.1	0.01
identified 2	1.233	0.2055	0.08563	0.04622
initial estimate 3	0.5	0.5	0.5	0.5
identified 3	0.8629	0.4480	0.09893	0.05622

Table 5

Lower bounds and upper bounds for the identification of Lim-Huh model parameters.

parameter	lower bound	upper bound
q_1	0.01	2
q_2	0.0001	0.5
q_3	0.01	0.8
m	0.01	0.3

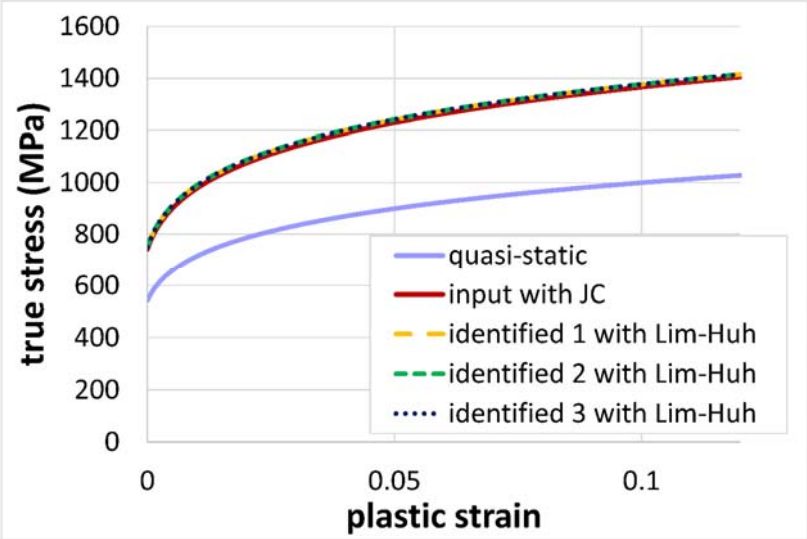

Fig. 12. Comparison of stress-strain curves between the input with Johnson-Cook model and the identified using the VFM with Lim-Huh model at the strain rate of 200 s^{-1}.

4. Experiment

4.1 Standard uniaxial tensile tests at quasi-static state

In this study, three DP steel sheet grades, DP590, DP780 and DP980 were investigated. In order to retrieve the dynamic parameters of Lim-Huh model, it is required to determine the true stress-plastic strain curves σ_r (see Eq. 6) from quasi-static tensile tests.

Tensile specimens with ASTM E8 were fabricated to carry out for quasi-static tensile tests. A MTS servo-hydraulic test system with a mechanical extensometer was utilized to obtain the engineering stress-strain curves. A quasi-static strain rate of 0.002 s^{-1} was selected for the tests. Then, the true stress-plastic strain curves were determined using the 0.2 % offset method up to the maximum uniform

elongation point. A curve fitting method was applied for each pre-necking true stress-plastic strain curve using several hardening models and a combination of Swift and modified Voce hardening laws in Eq. (12) which describes the hardening behaviors of three materials the best was selected.

$$\sigma_r = X_1\left(X_2 + \varepsilon_p\right)^{X_3} + X_4 + X_5\varepsilon_p + X_6\left(1 - \exp\left(-X_7\varepsilon_p\right)\right) \quad (12)$$

The corresponding hardening parameters at quasi-static strain rate are shown in Table 6.

Table 6

The hardening parameters at quasi-static strain rate (units for X_1, X_4, X_5, X_6: MPa).

material	X_1	X_2	X_3	X_4	X_5	X_6	X_7
DP590	474.1	0.001362	0.1369	151.2	393.6	136.1	35.74
DP780	442.9	8.974×10^{-5}	0.3046	440.6	696.9	261.9	64.76
DP980	640.4	0.0001022	0.1328	530.9	101.4	143.5	149.9

The curve-fitted true stress-plastic strain curves using the chosen hardening law are compared to the curves based on 0.2 % offset method in Fig. 13. The maximum plastic strains were 14 %, 11 % and 4.1 % for DP590, DP780 and DP980, respectively.

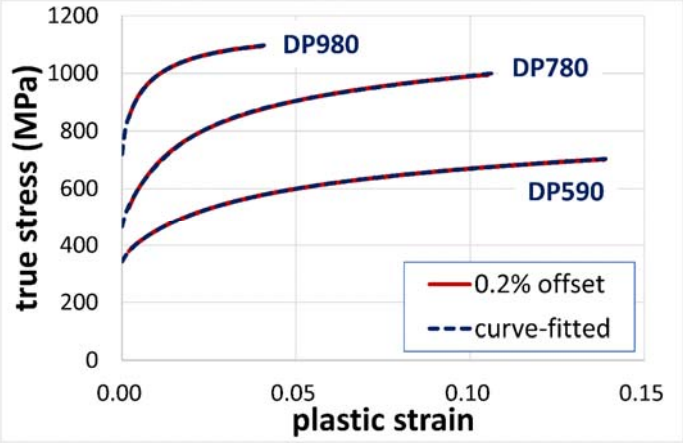

Fig. 13. Comparison of the true stress-plastic strain curves between 0.2 % offset method and curve-fitted.

4.2 Acquisition of load data

At high load rates, stress waves are generated which lead to significant acceleration levels. This causes the well-known issue of ringing in the load cells of standard test machines (Huh et al., 2009). Therefore, usually, strain gauges are attached to the elastic deformation region on the specimen for load calculation in practice (Bruce et al., 2004; Borsutzki et al., 2005; Xia et al., 2016).

In this study, strain gauges were attached to the specimen grip part where the deformation is linear elastic for load acquisition. As can be seen in Fig. 4, one grip side of the specimen at the fixed part is longer than the other side in order to induce uniform elastic deformation. The optimized length of the grip part and location of the strain gauges were carefully scrutinized using FE analyses.

It was found that the specimen vibrated in the vertical direction (direction normal to the sheet plane) during the experiments. To compensate the bending effect, strain gauges were attached to both sides of the specimen at the same position (front and back). Average of voltage signals from the strain gauges on both sides is shown in Fig. 14(a).

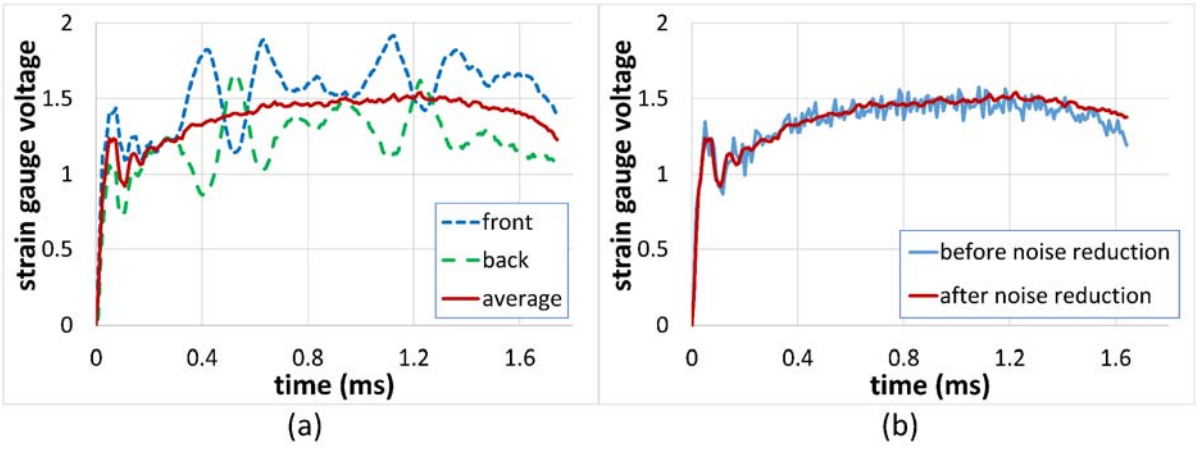

Fig. 14. Load data (a) average of voltage signals from the strain gauges (b) noise reduction.

Then, the elastic strain data was calculated from the average voltage and converted to load using Hooke's law.

$$F = AE\varepsilon \tag{13}$$

where F, A and E represent load, cross sectional area, and Young's modulus, respectively.

Young's moduli measured from quasi-static tensile tests were 209.1, 207.1 and 209.7 GPa for DP590,

DP780 and DP980, respectively. In addition, the modulus is required for the identification of dynamic hardening parameters in the VFM scheme. Consequently, the obtained Young's Modulus was used for the VFM analysis in the experiments.

Initially, the noise level in the load data was quite high as can be seen in Fig. 14(b). Therefore, in order to reduce noise level, a low-pass filter was used in the amplifier (Tokyo Sokki Kenkyujo, dynamic strainmeter DC-97A). As a result, the noise level was reduced significantly as shown in Fig. 14(b). The load data was recorded from the strain gauges by a data acquisition (DAQ) system simultaneously when images of speckle patterns were taken by the high-speed camera.

4.3 Temporal and spatial smoothing of noise

As discussed in (Kim et al., 2013), the experimental noise on the strain field measurement affects the stress calculation significantly in the VFM identification scheme. The noise effect is a serious issue in dealing with a rate dependent model because the second derivative of the equivalent plastic strain with respect to time $(d^2\varepsilon_p/dt^2)$ is required during the stress updating.

Both spatial and temporal smoothing methods were applied to lower the noise effects in this study. Basically, a smoothing technique is a low pass filtering which removes high frequency signal to enhance the signal-to-noise ratio (SNR). In spatial smoothing, filtering is applied to two-dimensional coordinates while temporal filtering is conducted with respect to time. In this study, the diffuse approximation (DA) method (Avril et al., 2008c) was used to perform spatial smoothing. The DA method utilizes local polynomial regression on the full-field displacements. The local filtering is carried out in the window with a chosen pixel radius. Here, the DA method with a radius of 10 was used. In addition, the moving average filter in Matlab was chosen to operate temporal smoothing. The moving average method takes the average of a certain number of successive data points around a specified point. Then, this specified point value is replaced with the new average value. In addition, a concern was to minimize over-smoothing of the original signal while removing high frequency noise. Thus, an averaging of five points for the moving average was selected on the consecutive strain data and the comparison of the results before and after applying temporal smoothing is shown in Fig. 15.

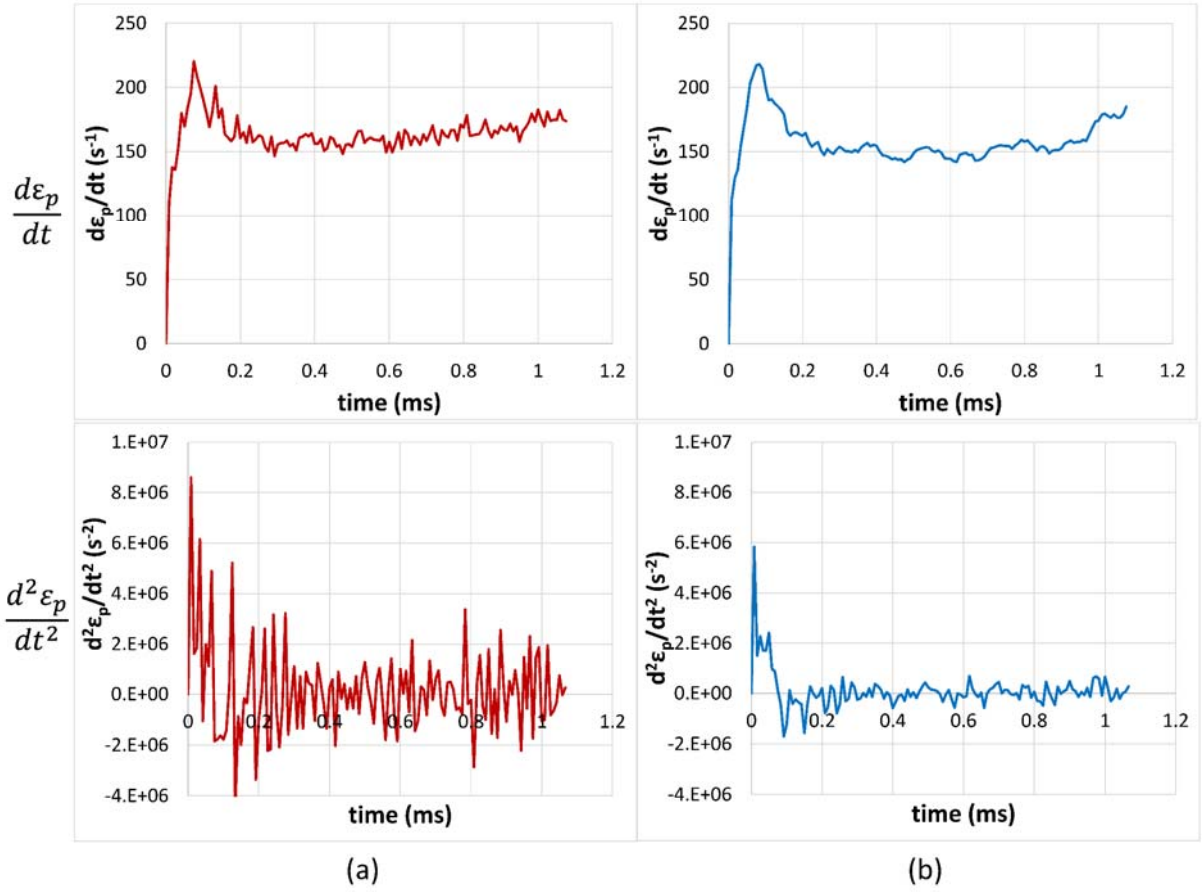

Fig. 15. Comparison of the results (a) before applying temporal smoothing (b) after applying temporal smoothing.

4.4 Experiment results with the VFM

For each material, three specimens were tested to check the reproducibility. Since it was found that the deviations for strain, strain rate and load data were small between the three specimens, the results for only one specimen for each material are presented for the sake of brevity.

4.4.1 Load and strain rate data

The measured load data obtained from the strain gauges is plotted as a function of time in Fig. 16.

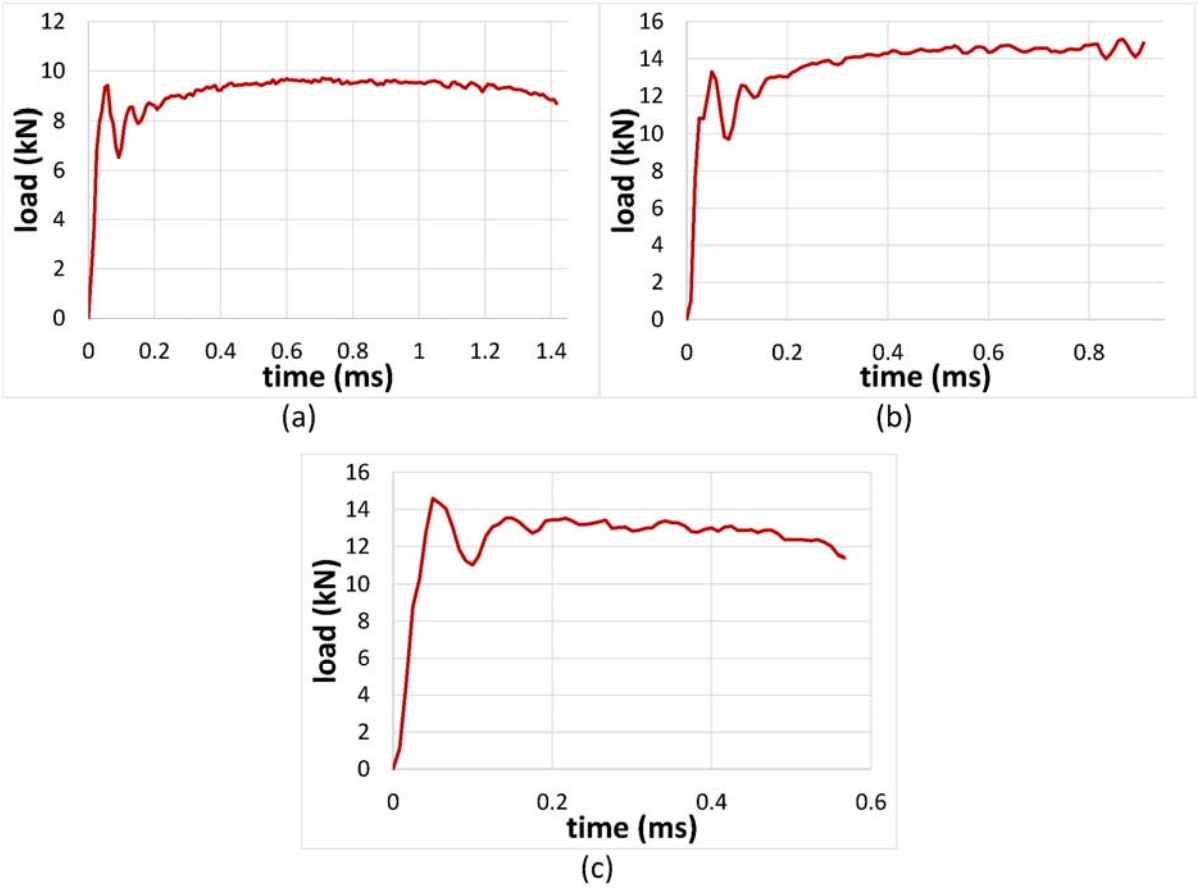

Fig. 16. Measured load data (a) DP590 (b) DP780 (c) DP980.

The evolution of the strain rates as a function of time for each material is presented in Fig. 17 and the evolution as a function of plastic strain is shown in Fig 18.

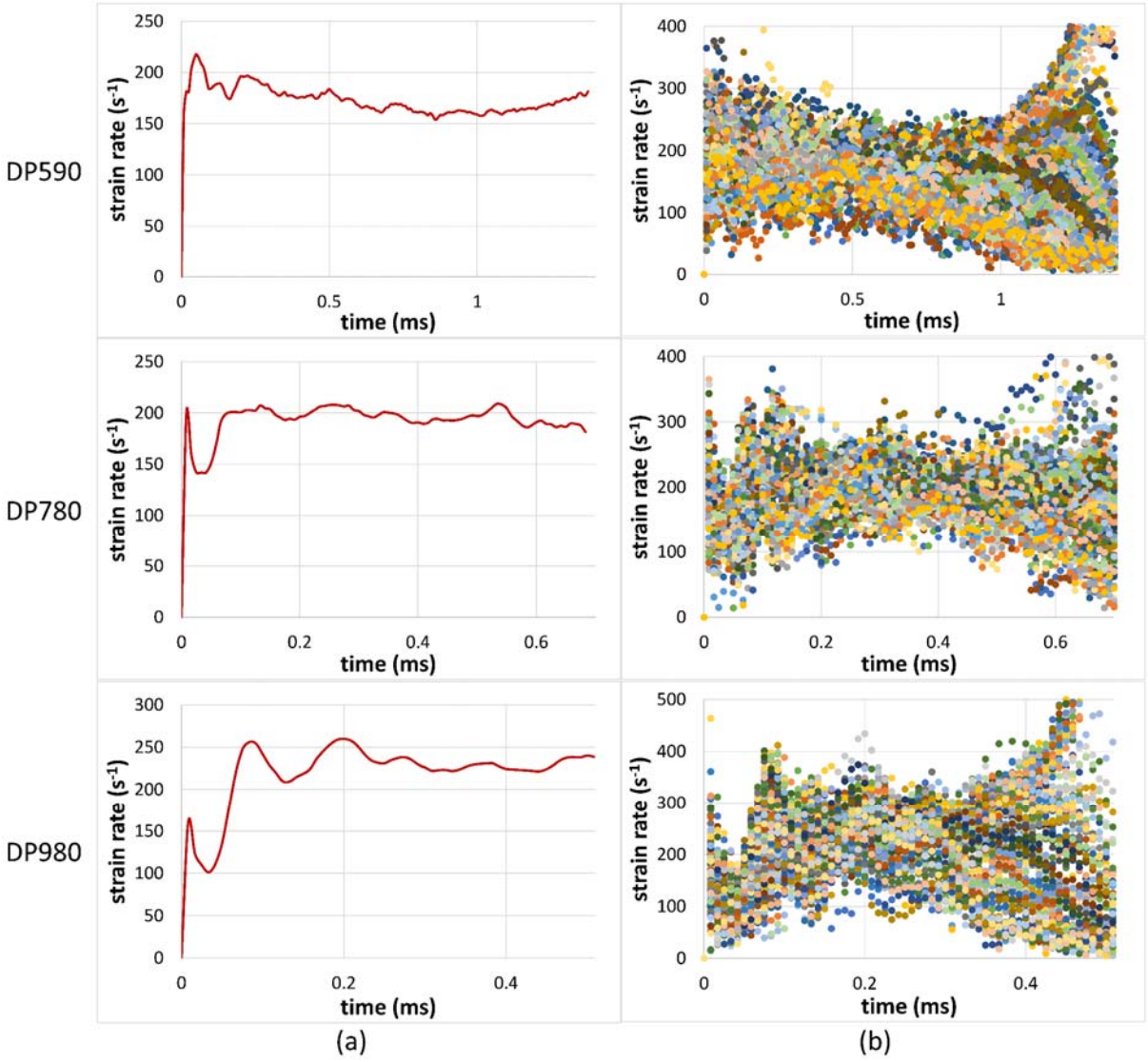

Fig. 17. Evolution of (a) AOI-averaged strain rate and (b) strain rate distribution as a function of time for each material.

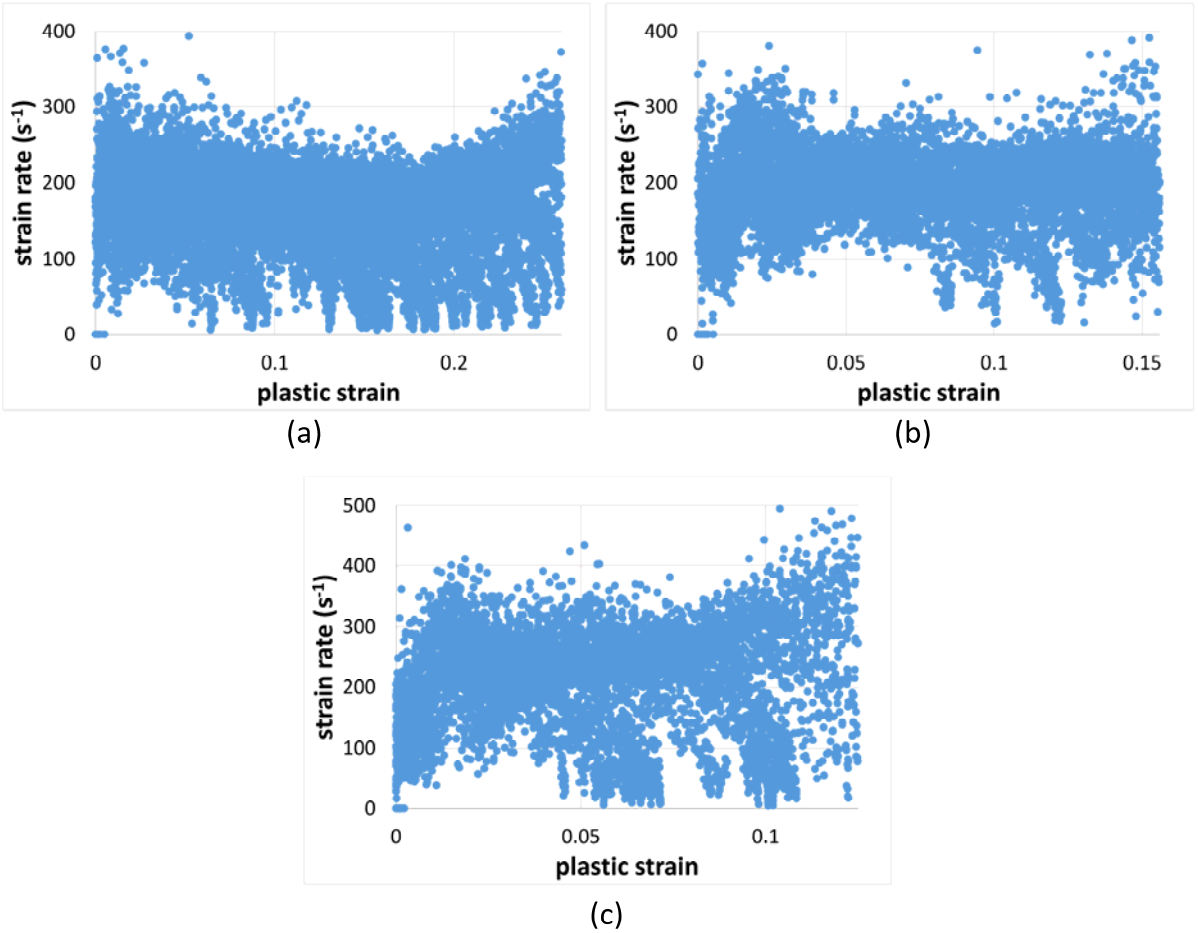

Fig. 18. Evolution of strain rate distribution as a function of plastic strain for each material (a) DP590 (b) DP780 (c) DP980.

It can be seen that heterogeneous strain rate information at intermediate strain rates can be obtained from a single experiment. The strain rate distribution gradually increases after around 1 ms, 0.5 ms, 0.3 ms due to diffuse necking for DP590, DP780, DP980, respectively as shown in Fig. 17(b). In addition, it was found that the average strain rate increases as the material strength increases at the same experimental condition. The approximate ranges of strain rate distribution before diffuse necking are listed in Table 7.

Table 7

Ranges of strain rate distribution (experiments).

material	range of strain rate distribution
DP590	100 s^{-1} - 250 s^{-1}
DP780	100 s^{-1} - 300 s^{-1}
DP980	100 s^{-1} - 350 s^{-1}

4.4.2 Identified results with the VFM

In order to identify the dynamic parameters of Lim-Huh model, all the experimental data shown in the previous sections was processed using the VFM, leading to the results listed in Table 8. Initial estimates of 0.1, 0.1, 0.1 and 0.1 were used to start the identification process. Although the hardening behavior can be characterized up to the initial stage of localized necking using the VFM (Kim et al., 2013), here the identification was performed only up to the uniform elongation. The dynamic parameters were identified in less than 10 min through an iteration procedure.

Table 8

Identified Lim-Huh model parameters from the VFM (experiments).

material	q_1	q_2	q_3	m
DP590	0.1045	0.001525	0.2236	0.08824
DP780	0.2748	0.0009023	0.1079	0.04393
DP980	0.07738	0.001483	0.4871	0.02095

The resulting stress-strain curves based on the determined Lim-Huh model parameters for strain rates of 100 s^{-1}, 200 s^{-1} and 300 s^{-1} are shown in Fig. 19 and compared with the quasi-static curves. The initial yield stress and flow stress at the selected strain rates are higher than those from the quasi-static strain rate and it can be seen that flow stress increases as strain rate increases.

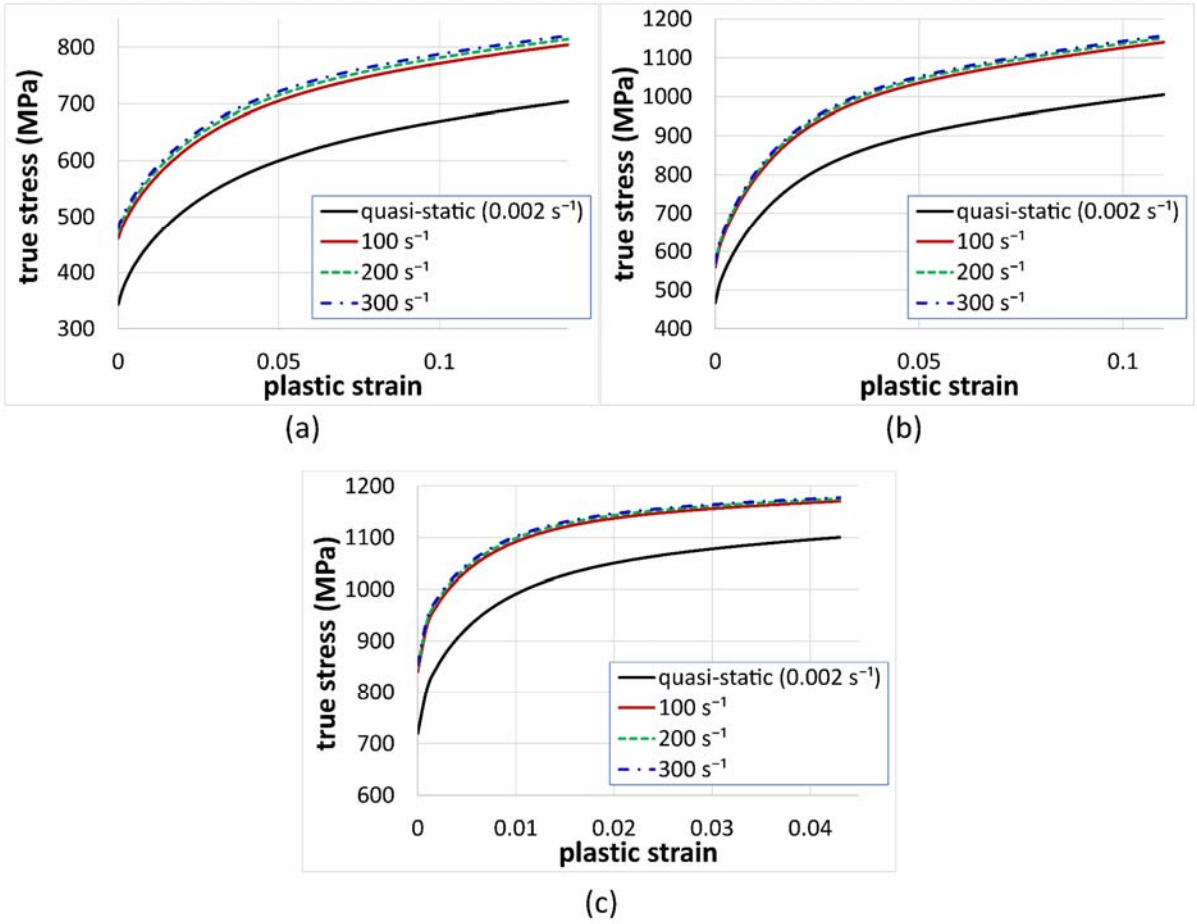

Fig. 19. The identified stress-strain curves at the chosen strain rates (a) DP590 (b) DP780 (c) DP980.

5. Discussion

5.1 Validation of the identified stress-strain curves with the VFM

In section 4.4.2, it was shown that the stress-strain curves at intermediate strain rates (100 s^{-1} – 300 s^{-1}) were obtained from a single experiment using the VFM. However, a still unanswered question is the reliability of the identified curves. The aim of this section is to validate these identified stress-strain curves. For DP780, the average strain rate in the experiment was about 200 s^{-1}, so the determined curve with Lim-Huh model at the strain rate of 200 s^{-1} is compared with the true stress-plastic strain curve obtained from the load data using 0.2 % offset method (like in a quasi-static test) in Fig. 20. Though the stress-strain curve from 0.2 % offset method is a bit fluctuating, two curves are in good agreement.

In addition, the load-displacement curve was obtained from simulated measurements based on the

FE model described in section 3.1. The identified parameter of Johnson-Cook model for DP780 in section 5.4 was fed into the FE simulations since the predicted hardening curves are very close to each other between Johnson-Cook and Lim-Huh models for DP780 and Johnson-Cook model is implemented in Abaqus. The simulated load-displacement curve is compared with the curve from experiments in Fig. 21 and it can be seen that two curves are also in good agreement. Therefore, it is considered that the identification results using the VFM with Lim-Huh model are satisfactory.

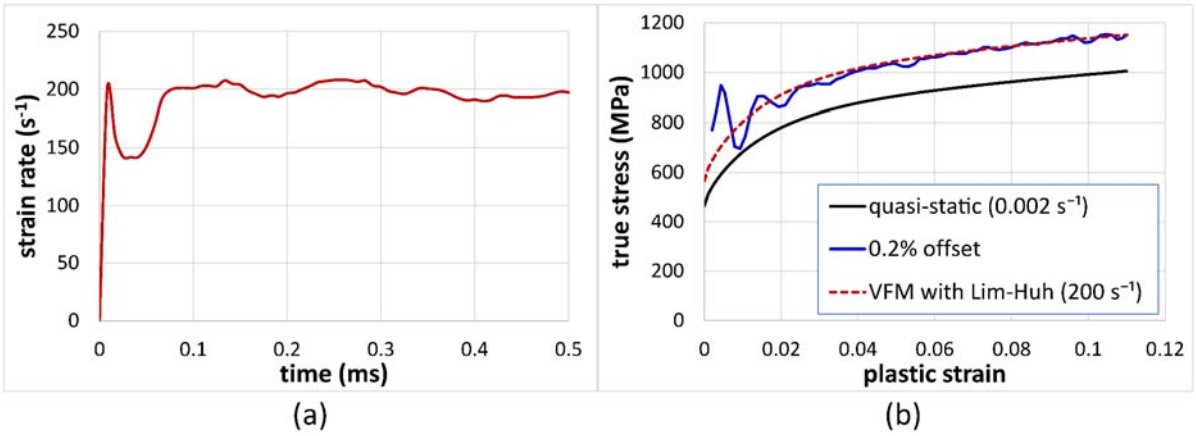

Fig. 20. Validation of the identified stress-strain curve of DP780 with the VFM (a) AOI-averaged strain rate (b) comparison of the stress-strain curves between by the VFM and by 0.2 % offset method.

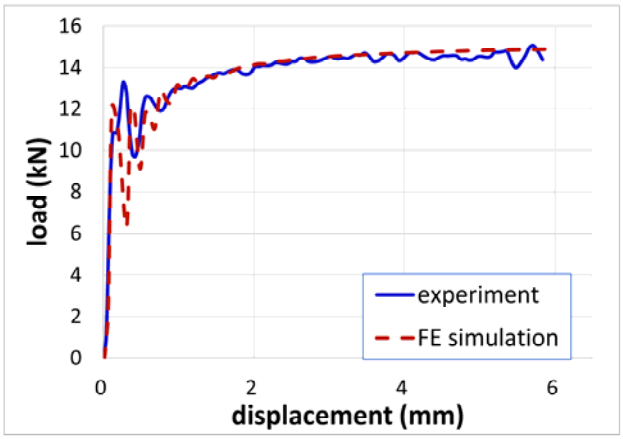

Fig. 21. Comparison of load-displacement curves for DP780.

5.2 Effect of hardening law at quasi-static

As discussed in section 4.1, the quasi-static true stress-strain curves are required to determine Lim-

Huh model parameters using the VFM, which means that the chosen hardening law may affect the identified Lim-Huh curves. In order to investigate the effect of quasi-static hardening curves, two different hardening models, Swift hardening and combination of Swift and modified Voce hardening were used to identify Lim-Huh parameters. The curve-fitting results to the quasi-static pre-necking true stress-strain curve of DP780 using two hardening laws are shown in Fig. 22(a) and Fig. 22(b). Discrepancy is a bit larger in the case of Swift fitting. Fig. 22(c) compares the identified dynamic curves with the Lim-Huh model. Although the two curves are close from each other, it was found that the observed deviation of the quasi-static curves is reflected in the dynamic curves identified with the VFM.

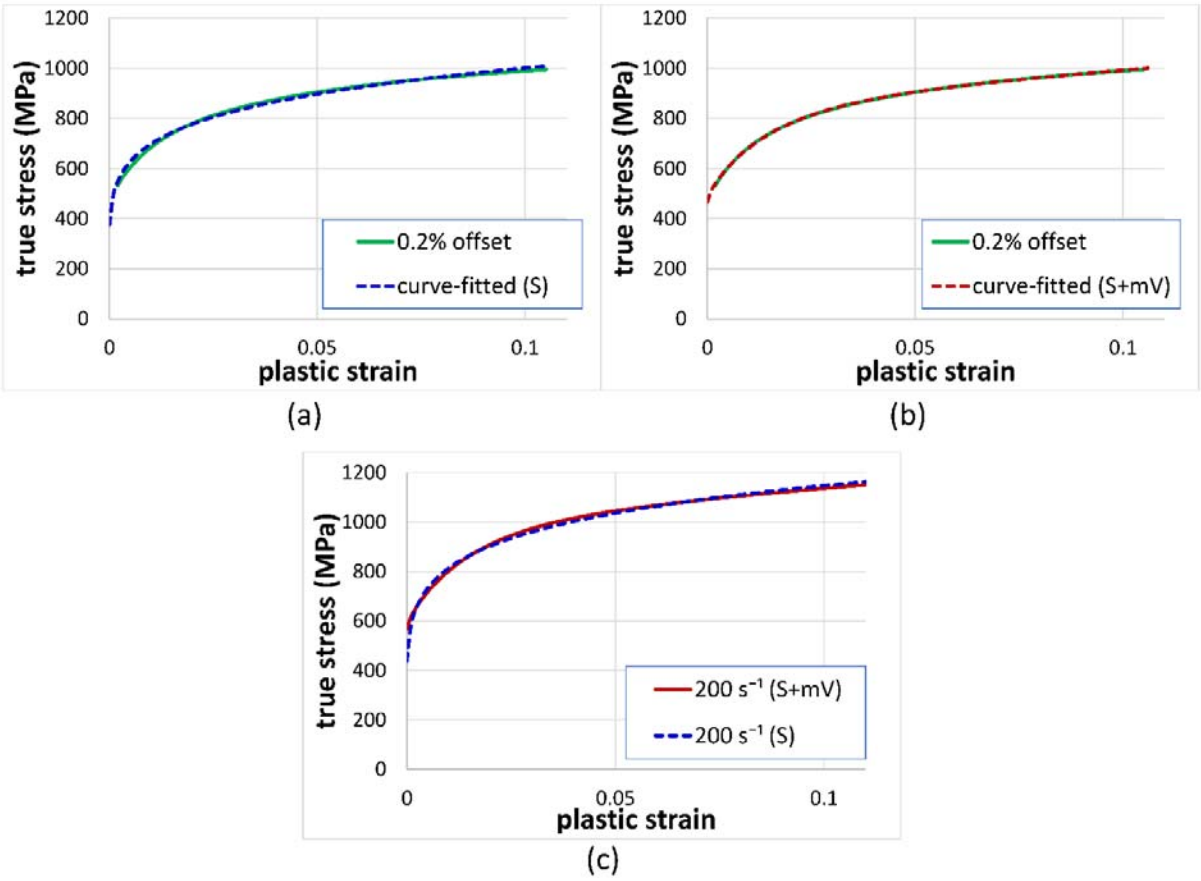

Fig. 22. Effect of quasi-static hardening law: curve-fitting with (a) Swift and (b) combination of Swift and modified Voce (c) identified Lim-Huh curves at 200 s^{-1} using the two hardening laws (DP780, S: Swift, S+mV: Swift and modified Voce).

5.3 Effect of smoothing

As shown in section 4.3, both spatial and temporal smoothing methods were adopted to decrease the noise effects. In this section, the effect of smoothing on the VFM identification results is discussed.

Different number of averaging points for the moving average (temporal smoothing) and different radius size for the DA (spatial smoothing) were used for the identification of Lim-Huh model for DP780 at the strain rate of 200 s^{-1} and the results are shown in Fig. 23. It should be noted here that the identification procedure did not converge when the temporal smoothing was not applied because the second derivative of the equivalent plastic strain with respect to time $(d^2\varepsilon_p/dt^2)$ is very noisy as shown in Fig. 15. However, in other cases, the identification results are not very different regardless of temporal and spatial smoothing parameters. In the case of temporal smoothing, the initial yield stress decreases slightly when the number of averaging points increases, whereas the flow stresses are almost the same. In addition, the flow stress decreases slightly when the radius size of the DA for spatial smoothing increases. The maximum relative difference of flow stresses between cases without spatial smoothing and with radius size of 15 for the DA is less than 1.5 %.

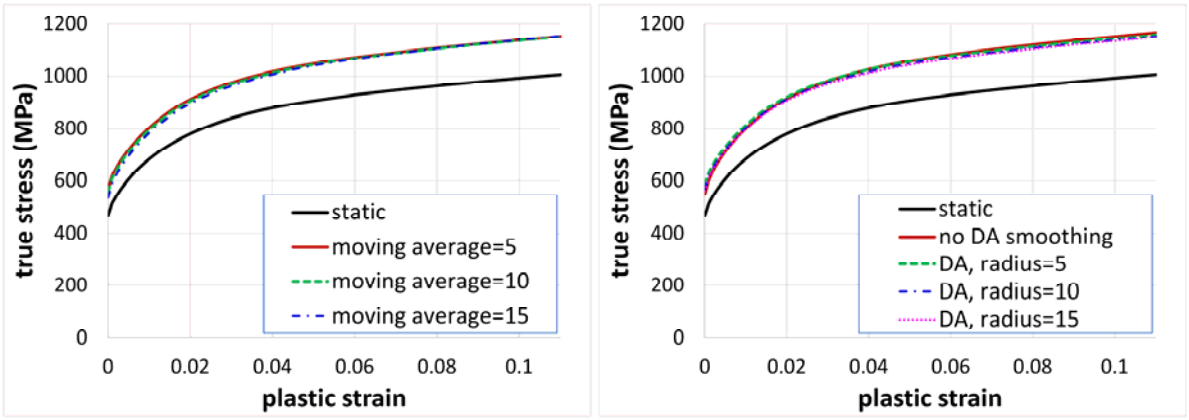

Fig. 23. Effect of smoothing on the VFM identification results (identified Lim-Huh curves at the strain rate of 200 s^{-1}, DP780): (a) temporal smoothing effect with different averaging points (DA, radius=10) and (b) spatial smoothing effect with different DA radius size (moving average=5).

It is considered that the least squares regression method to calculate the logarithmic strain fields shown in section 2.2 performs spatial smoothing of the experimental noise well in this case because a larger size of the triangular elements was used in this study compared to the analyses adopted in (Kim et al., 2013; Kim et al., 2014).

5.4 Comparison between Lim-Huh and Johnson-Cook models

Before closing, it is worth comparing the Lim-Huh and Johnson-Cook models. The same VFM identification procedure was applied to determine the parameter of the Johnson-Cook model for the three materials. The identified Johnson-Cook parameters are listed in Table 9. Then, the identified curves of Lim-Huh and Johnson-Cook models are compared for the strain rate of 200 s^{-1} in Fig. 24.

It is generally observed that the initial yield stress is lower and hardening rate is higher for Johnson-Cook model. For DP590 and DP980, the initial yield stress at 200 s^{-1} is close to that of the quasi-static for Johnson-Cook model. Nonetheless, the predicted Johnson-Cook hardening curves for the DP materials are not very different from those of the Lim-Huh model considering the number of strain rate sensitivity (one for Johnson-Cook and four for Lim-Huh).

It was reported that strain hardening rate tends to decrease when strain rate increases for automotive steels at intermediate strain rates, however, strain hardening rate increases as strain rate increases for Johnson-Cook model (Lim, 2005; Huh et al., 2014). In this study, this behavior of Johnson-Cook model was not observed due to the restricted range of strain rates and number of materials.

Table 9

Identified Johnson-Cook parameters from the VFM (experiments).

material	C
DP590	0.01504
DP780	0.01282
DP980	0.006864

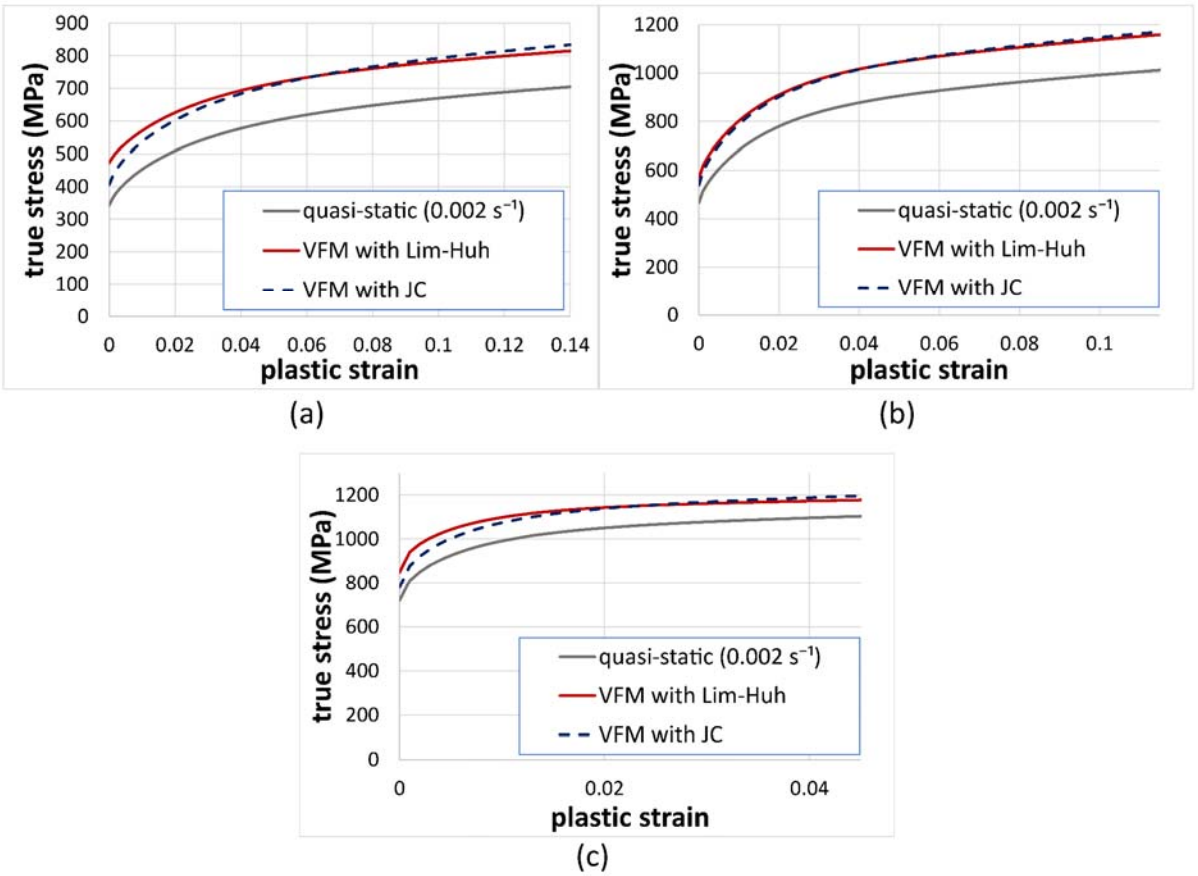

Fig. 24. Comparison of the identified curves at the strain rate of 200 s^{-1} between Lim-Huh and Johnson-Cook models (a) DP590 (b) DP780 (c) DP980.

6. Conclusion

In the past, a large number of experiments have been usually performed to derive the stress-strain curves at various strain rates, which is costly and time consuming. Furthermore, in order to solve the varying strain rate problem, complicated data processing for significant amount of experimental data was required. The present study proposed a new method to overcome the problems efficiently. This study utilized an inverse identification method with a rate dependent hardening law and the full-field measurement technique to derive the stress-strain curves of advanced high strength steels at intermediate strain rates from a single dynamic experiment. A new type of high-speed tensile tester for sheet metal specimens was built and the dynamic behavior was captured by a digital image correlation technique using a high-speed camera. The virtual fields method (VFM) was adopted as an inverse identification scheme to retrieve dynamic parameters of an advanced rate dependent hardening model

from the dynamic experimental data. The stress-strain curves of three dual phase steels (DP590, DP780, DP980) at intermediate strain rates (100 s^{-1} – 300 s^{-1}) were obtained from a single experiment. The main observations and conclusions of the current work are as follows:

(1) The main idea of determining the stress-strain curves for various strain rates from a single experiment was based on the observation that the strain rate distribution is heterogeneous over the area of interest of the specimen. This indicates that this rich strain rate information can be used for the VFM to identify strain rate dependence with an appropriate rate dependent model.

(2) For the experiments, a novel high-speed tensile tester for sheet metals was developed and the gripping of the specimen was modified to provide a sharper loading pulse. This tester with the new gripping generated intermediate strain rates of up to 300 s^{-1} for advanced high strength steel specimens.

(3) The Lim-Huh model was chosen as an advanced rate dependent hardening law. In order to validate the identified stress-strain curves of the Lim-Huh model using the VFM, the determined curve with the Lim-Huh model at the strain rate of 200 s^{-1} was compared with the true stress-plastic strain curve obtained from the load data using 0.2 % offset method. Two curves were in good agreement, indicating that the identification results using the VFM with the Lim-Huh model are very reliable.

(4) The identified curves of Lim-Huh and Johnson-Cook models were compared for the strain rate of 200 s^{-1}. The Johnson-Cook hardening curves for the DP materials are not very different from those of the Lim-Huh model though the initial yield stress is lower and hardening rate is higher for Johnson-Cook model.

Promising results were obtained for characterizing the dynamic behavior at intermediate strain rates efficiently. The potential of this methodology is that the number of expensive and complicated experiments can be reduced significantly by optimizing the specimen geometry which can provide very heterogeneous strain rate information. However, very accurate experimentation with full-field deformation measurements would be required as a specific difficulty in this case since highly heterogeneous strain rate information should be acquired from a single experiment.

The current technique will be applied to notched specimens to increase the strain rate range (currently, 100 s^{-1} – 300 s^{-1}). In addition, identification of the Lim-Huh parameters with the VFM at higher strain

rates (at around 1000 s^{-1}) will be investigated. At such strain rates, accurate measurement of load data is difficult due to the inertial effect, the identification will be carried out using the acceleration data without utilizing load information.

Acknowledgement

The authors appreciate the generous support by POSCO (Pohang Iron and Steel Company). Prof. Pierron acknowledges the support of EPSRC through grant EP/L026910/1.

Appendix A

Let us assume a stress function as a function of the strain and the strain rate, that is $\sigma = \sigma(\varepsilon, \dot{\varepsilon})$. The differential is expressed as

$$d\sigma = \frac{\partial \sigma}{\partial \varepsilon} d\varepsilon + \frac{\partial \sigma}{\partial \dot{\varepsilon}} d\dot{\varepsilon} \tag{A.1}$$

The infinitesimal variations $d\varepsilon$ and $d\dot{\varepsilon}$ are expressed as a function of time as

$$d\varepsilon = \dot{\varepsilon} dt \tag{A.2a}$$

$$d\dot{\varepsilon} = \ddot{\varepsilon} dt \tag{A.2b}$$

The ratio of these two expressions leads to

$$\frac{d\dot{\varepsilon}}{d\varepsilon} = \frac{\ddot{\varepsilon}}{\dot{\varepsilon}} \tag{A.3}$$

Then, the stress differential can be rearranged

$$d\sigma = \left(\frac{\partial \sigma}{\partial \varepsilon} + \frac{\partial \sigma}{\partial \dot{\varepsilon}} \frac{d\dot{\varepsilon}}{d\varepsilon}\right) d\varepsilon = \left(\frac{\partial \sigma}{\partial \varepsilon} + \frac{\partial \sigma}{\partial \dot{\varepsilon}} \frac{\ddot{\varepsilon}}{\dot{\varepsilon}}\right) d\varepsilon \tag{A.4}$$

Now, as an application, let us assume a very simple rate dependent hardening law

$$\sigma_s = \sigma_r(\varepsilon_p) \dot{\varepsilon}_p^m \tag{A.5}$$

where $\sigma_r(\varepsilon_p)$ can be any hardening equation, $\dot{\varepsilon}_p$ the equivalent plastic strain rate and m is the strain rate sensitivity. Then, the two partial derivatives become

$$\frac{\partial \sigma_s}{\partial \varepsilon_p} = \sigma_r' \dot{\varepsilon}_p^m \tag{A.6a}$$

$$\frac{\partial \sigma_s}{\partial \dot{\varepsilon}_p} = m\sigma_r \dot{\varepsilon}_p^{m-1} = m\sigma_r \frac{\dot{\varepsilon}_p^m}{\dot{\varepsilon}_p} \tag{A.6b}$$

with $\sigma_r' = d\sigma_r / d\varepsilon_p$. Substituting in Eq. (A.4), this leads to the stress differential

$$d\sigma_s = \left(\sigma_r' \dot{\varepsilon}_p^m + m\sigma_r \frac{\dot{\varepsilon}_p^m}{\dot{\varepsilon}_p} \frac{\ddot{\varepsilon}_p}{\dot{\varepsilon}_p} \right) d\varepsilon_p = \sigma_r \dot{\varepsilon}_p^m \left(\frac{\sigma_r'}{\sigma_r} + m \frac{\ddot{\varepsilon}_p}{\dot{\varepsilon}_p^2} \right) d\varepsilon_p \tag{A.7}$$

Finally,

$$d\sigma_s = \sigma_s \left(\frac{\sigma_r'}{\sigma_r} + m \frac{\ddot{\varepsilon}_p}{\dot{\varepsilon}_p^2} \right) d\varepsilon_p \tag{A.8}$$

In the present work, the Swift hardening function $\sigma_r(\varepsilon_p) = X_1 \left(X_2 + \varepsilon_p \right)^{X_3}$ is employed to describe the strain hardening curve, and the stress differential reduces to

$$d\sigma_s = X_1 \left(X_2 + \varepsilon_p \right)^{X_3} \dot{\varepsilon}_p^m \left(\frac{X_3}{X_2 + \varepsilon_p} + m \frac{\ddot{\varepsilon}_p}{\dot{\varepsilon}_p^2} \right) d\varepsilon_p \tag{A.9}$$

References

Avril, S., Pierron, F., Pannier, Y., Rotinat, R., 2008a. Stress reconstruction and constitutive parameter identification in plane-stress elasto-plastic problems using surface measurements of deformation fields. Exp. Mech. 48 (4), 403-419. https://doi.org/10.1007/s11340-007-9084-2.

Avril, S., Pierron, F., Sutton, M. A., Yan, J., 2008b. Identification of elasto-visco-plastic parameters and characterization of Lüders behavior using digital image correlation and the virtual fields method. Mech. Mater. 40 (9), 729-742. https://doi.org/10.1016/j.mechmat.2008.03.007.

Avril, S., Feissel, P., Pierron, F., Villon, P., 2008c. Estimation of the strain field from full-field displacement noisy data: comparing finite elements global least squares and polynomial diffuse approximation. Eur. J. Comput. Mech. 17 (5-7), 857-868. https://doi.org/10.3166/remn.17.857-868.

Bae, G., 2013. Strain rate-dependent flow stress curves in the large deformation range. AIP Conference Proceedings 1567 (1), 504-507. American Institute of Physics. https://doi.org/10.1063/1.4850022.

Borsutzki, M., Cornette, D., Kuriyama, Y., Uenishi, A., Yan, B., Opbroek, E., 2005. Recommendations for dynamic tensile testing of sheet steels. Int. Iron Steel Inst., 30.

Bouda, P., Langrand, B., Notta-Cuvier, D., Markiewicz, E., Pierron, F., 2019. A computational approach to design new tests for viscoplasticity characterization at high strain-rates. Comput. Mech. 64 (6), 1639-1654. https://doi.org/10.1007/s00466-019-01742-y.

Bruce, D. M., Matlock, D. K., Speer, J. G., De, A. K., 2004. Assessment of the strain-rate dependent tensile properties of automotive sheet steels (No. 2004-01-0507). SAE Technical Paper. https://doi.org/10.4271/2004-01-0507.

Chen, W.-F., 1994. Constitutive Equations for Engineering Materials. Plasticity and Modeling, vol. 2. Elsevier.

Dunne, F., Petrinic, N., 2005. Introduction to computational plasticity. Oxford University Press.

Field, J. E., Walley, T. M., Proud, W. G., Goldrein, H. T., Siviour, C. R., 2004. Review of experimental techniques for high rate deformation and shock studies. Int. J. Impact Eng. 30 (7), 725-775. https://doi.org/10.1016/j.ijimpeng.2004.03.005.

Fletcher, L., Davis, F., Dreuilhe, S., Marek, A., Pierron, F., 2021. High strain rate elasto-plasticity identification using the image-based inertial impact (IBII) test part 2: Experimental validation. Strain, 57(2), e12374. https://doi.org/10.1111/str.12374.

Fourest, T., Bouda, P., Fletcher, L. C., Notta-Cuvier, D., Markiewicz, E., Pierron, F., Langrand, B., 2020. Image-based inertial impact test for characterisation of strain rate dependency of Ti6al4v titanium alloy. Exp. Mech. 60 (2), 235-248. https://doi.org/10.1007/s11340-019-00559-3.

Fu, J., Barlat, F., Kim, J. H., Pierron, F., 2017. Application of the virtual fields method to the identification of the homogeneous anisotropic hardening parameters for advanced high strength steels. Int. J. Plast. 93, 229-250. https://doi.org/10.1016/j.ijplas.2016.07.013.

Grama, S. N., Subramanian, S. J., Pierron, F., 2015. On the identifiability of Anand visco-plastic model parameters using the Virtual Fields Method. Acta Mater. 86, 118-136. https://doi.org/10.1016/j.actamat.2014.11.052.

Grédiac, M., Pierron, F., 2006. Applying the virtual fields method to the identification of elasto-plastic constitutive parameters. Int. J. Plast. 22 (4), 602-627. https://doi.org/10.1016/j.ijplas.2005.04.007.

Huh, H., Lim, J. H., Park, S. H., 2009. High speed tensile test of steel sheets for the stress-strain curve

at the intermediate strain rate. Int. J. Automot. Technol. 10 (2), 195-204. https://doi.org/10.1007/s12239−009−0023−3.

Huh, H., Ahn, K., Lim, J. H., Kim, H. W., Park, L. J., 2014. Evaluation of dynamic hardening models for BCC, FCC, and HCP metals at a wide range of strain rates. J. Mater. Process. Technol. 214 (7), 1326-1340. https://doi.org/10.1016/j.jmatprotec.2014.02.004.

Kim, J. H., Serpantié, A., Barlat, F., Pierron, F., Lee, M. G., 2013. Characterization of the post-necking strain hardening behavior using the virtual fields method. Int. J. Solids Struct. 50 (24), 3829-3842. https://doi.org/10.1016/j.ijsolstr.2013.07.018.

Kim, J. H., Barlat, F., Pierron, F., Lee, M. G., 2014. Determination of anisotropic plastic constitutive parameters using the virtual fields method. Exp. Mech. 54 (7), 1189-1204. https://doi.org/10.1007/s11340-014-9879-x.

Koohbor, B., Kidane, A., Lu, W. Y., 2016. Effect of specimen size, compressibility and inertia on the response of rigid polymer foams subjected to high velocity direct impact loading. Int. J. Impact Eng. 98, 62-74. https://doi.org/10.1016/j.ijimpeng.2016.08.006.

Koohbor, B., Kidane, A., Sutton, M. A., Zhao, X., Mallon, S., 2017. Analysis of dynamic bending test using ultra high speed DIC and the virtual fields method. Int. J. Impact Eng. 110, 299-310. https://doi.org/10.1016/j.ijimpeng.2016.12.021.

Le Louëdec, G., Pierron, F., Sutton, M. A., Siviour, C., Reynolds, A. P., 2015. Identification of the dynamic properties of Al 5456 FSW welds using the virtual fields method. J. Dyn. Behav. Mater. 1 (2), 176-190. https://doi.org/10.1007/s40870-015-0014-6.

Lim, J. H., 2005. Study on dynamic tensile tests of auto-body steel sheet at the intermediate strain rate for material constitutive equations. Ph.D. dissertation. KAIST, Republic of Korea.

Longana, M. L., Dulieu-Barton, J. M., Pierron, F., Syngellakis, S., 2009. Identification of constitutive properties of composite materials under high strain rate loading using optical strain measurement techniques. Technol. 20 (6), 062001.

Notta-Cuvier, D., Langrand, B., Markiewicz, E., Lauro, F., Portemont, G., 2013. Identification of Johnson-Cook's viscoplastic model parameters using the Virtual Fields Method: application to

Titanium alloy Ti6Al4V. Strain 49 (1), 22-45. https://doi.org/10.1111/str.12010.

POSCO, 2014. Automotive Steel Data Book. http://product.posco.com

Pierron, F., Avril, S., Tran, V. T., 2010. Extension of the virtual fields method to elasto-plastic material identification with cyclic loads and kinematic hardening. Int. J. Solids Struct. 47 (22-23), 2993-3010. https://doi.org/10.1016/j.ijsolstr.2010.06.022.

Pierron, F., Sutton, M. A., Tiwari, V., 2011. Ultra high speed DIC and virtual fields method analysis of a three point bending impact test on an aluminium bar. Exp. Mech. 51 (4), 537-563. https://doi.org/10.1007/s11340-010-9402-y.

Pierron, F., Grédiac, M., 2012. The virtual fields method: extracting constitutive mechanical parameters from full-field deformation measurements. Springer New York. https://doi.org/10.1007/978-1-4614-1824-5.

Pierron, F., Zhu, H., Siviour, C., 2014. Beyond Hopkinson's bar. Philos. T. Roy. Soc. A 372 (2023), 20130195. https://doi.org/10.1098/rsta.2013.0195.

Rossi, M., Pierron, F., 2012. Identification of plastic constitutive parameters at large deformations from three dimensional displacement fields. Comput. Mech. 49 (1), 53-71. https://doi.org/10.1007/s00466-011-0627-0.

Seghir, R., Pierron, F., 2018. A novel image-based ultrasonic test to map material mechanical properties at high strain-rates. Exp. Mech. 58 (2), 183-206. https://doi.org/10.1007/s11340-017-0329-4.

Sutton, M. A., Deng, X., Liu, J., Yang, L., 1996. Determination of elastic-plastic stresses and strains from measured surface strain data. Exp. Mech. 36 (2), 99-112. https://doi.org/10.1007/BF02328705.

Sutton, M. A., Orteu, J. J., Schreier, H., 2009. Image correlation for shape, motion and deformation measurements: basic concepts, theory and applications. Springer New York. https://doi.org/10.1007/978-0-387-78747-3.

Tran, T. K., Kim, D. J., 2012. Strain energy frame impact machine (SEFIM). J. Adv. Concr. Technol. 10 (3), 126-136. https://doi.org/10.3151/jact.10.126.

Xia, Y., Zhu, J., Wang, K., Zhou, Q., 2016. Design and verification of a strain gauge based load sensor

for medium-speed dynamic tests with a hydraulic test machine. Int. J. Impact Eng. 88, 139-152. https://doi.org/10.1016/j.ijimpeng.2015.10.004.